SUPPLEMENTAL INFORMATION

Association of impaired neuronal migration with cognitive deficits in extremely preterm infants

Ken-ichiro Kubo[#*], Kimiko Deguchi[#], Taku Nagai, Yukiko Ito, Keitaro Yoshida Toshihiro Endo, Seico Benner, Wei Shan, Ayako Kitazawa, Michihiko Aramaki, Kazuhiro Ishii, Minkyung Shin, Yuki Matsunaga, Kanehiro Hayashi, Masaki Kakeyama, Chiharu Tohyama, Kenji F. Tanaka, Kohichi Tanaka, Sachio Takashima, Masahiro Nakayama, Masayuki Itoh, Yukio Hirata, Barbara Antalffy, Dawna D. Armstrong, Kiyofumi Yamada, Ken Inoue*, Kazunori Nakajima*

#These two authors equally contributed to this work.
*Corresponding authors

This PDF file includes:

Supplemental Methods
Supplemental Tables 1-7
Supplemental Figures 1-17
Supplemental References

Supplemental Methods

Neuropathology.

Formalin fixed brain specimens from a cerebral hemisphere, usually from the frontal lobe, that included the ventricular zone and overlying white matter and cortex, were prepared for histological examination and immunohistochemical staining by standard protocols (71) and by using hematoxylin-eosin (HE), primary antibodies against GFAP (rabbit polyclonal, 1:1000, Chemicon, AB5804), Hu (human polyclonal, 1:1000, a gift from Dr. Hideyuki Okano, Keio University School of Medicine, Tokyo, Japan (25)), MAP2 (mouse monoclonal, 1:800, Sigma, M4403), NeuN (mouse monoclonal, 1:50, Chemicon, MAB377), Musashi1 (rat monoclonal, 1:1000, a gift from Dr. Hideyuki Okano (72)), nestin (rabbit polyclonal, 1:1000, a gift from Dr. Hideyuki Okano (73)), vimentin (mouse monoclonal, 1:20, DAKO, V9), CUX1 (CULT1, mouse monoclonal, 1:100, Abnova, H00001523-M01, as previously reported (29)), and by performing TUNEL (Chemicon, ApopTag kit, S7100). Controls for immunochemistry were prepared without using the primary antibody. Bright-field images acquired through microscopes (BZ-9000 and BZ-X700, Keyence, Osaka, Japan and NY-D5200 Supersystem, Microscope Network, Kawaguchi, Japan). Fluorescent images were acquired through confocal microscopes (FV1000, Olympus Optical, Tokyo, Japan).

For quantification of the cells showing positive staining for MAP2 or NeuN in the white matter, we counted the number of cells in the white matter from 10 randomly acquired digitized bright-field images (x20) of the fronto-temporal neocortex acquired with the BZ-X700 microscope (BZ-X700, Keyence, Osaka, Japan) (Figure 3 and Supplementary Figures 5 and 6). Examples of such bright-field images are shown in Supplemental Figure 6B.

To examine the extent of disruption of the VZ/SVZ/ependymal epithelium, we measured the degree of the disruption of the ventricular surface in the extremely preterm infants with WMI by dividing the length of the disrupted ventricular surface by the total length of the ventricular surface in each section (Supplementary Table 5 and Supplementary Figure 4).

Mice.

All animal experiments were performed using protocols approved by the Keio

University Institutional Animal Care and Use Committee, Nagoya University Institutional Animal Care and Use Committee, and Tokyo Medical and Dental University Institutional Animal Care and Use Committee in accordance with Institutional Guidelines on Animal Experimentation at Keio University, Nagoya University, Tokyo Medical and Dental University, and the Japanese Government Law Concerning the Protection and Control of Animals and Japanese Government Notification of Feeding and Safekeeping of Animals. Pregnant ICR or C57BL/6NCr (for gene microarray analysis, Supplemental Table 7 and Supplemental Figure 10) mice were purchased from Japan SLC (Shizuoka, Japan). Embryonic day 19 was designated postnatal day 0 (P0). Dams, pups, and weaned animals were housed under a 12 h light/dark cycle in a temperature-controlled room. The animals were given free access to food and water, except during behavioral experiments. Animals were weaned at 3 weeks of age, at which time males were separated from females. All behavioral tests were carried out with male mice at 6-7 weeks of age.

In utero electroporation.

Pregnant mice were deeply anesthetized with pentobarbital sodium (Nembutal), and their intrauterine embryos were surgically manipulated as described previously (74-76). A 1-2 μl volume of plasmid solution was injected into each lateral ventricle, and *in utero* electroporations was performed. A modified chicken β-actin promoter with cytomegalovirus-immediate early enhancer (CAG) promoter (provided by Dr. Junichi Miyazaki, Osaka University, Osaka, Japan (77))-driven green fluorescent protein (GFP) expression vector (pEGFP-CAGGS1, a GFP-plasmid) or a CAG promoter-driven tandem-Tomato fluorescent protein (tdTomato) expression vector (pCAG-tdTomato) (33) was injected at a concentration of 1.0 mg/ml. To generate mice that expressed the hM3Dq-mCherry in the mPFC, pCAGGS1-hM3Dq-mCherry (33) and pEGFP-CAGGS were co-transfected at a concentration of 3.0 mg/ml and 1.0 mg/ml, respectively.

Maternal uterine artery occlusion.

At E16.5 pregnant mice were deeply anesthetized with pentobarbital sodium (Nembutal), and their uterine arteries were occluded with clips used for human vascular surgery (Disposable Vascular Clip, BEAR Medic Corporation, TIS-1, Single type, Vein, Small, 20gf / 0.2N) to induce brain injury in the embryonic mouse brains, and the clips

were removed 14 min later. While the uterine arteries were occluded, the dams were maintained in the supine position on a warmer set at 37.5°C, except when set at 25.5°C for the maternal mild hypothermia experiments shown in Figure 9 and Supplemental Figure 17 (the experimental procedures are schematically shown in Supplemental Figure 17). In the sham operations of the control group, the uterine arteries were gently clipped, and the clips were immediately removed. Surface temperatures of the uterine horns were measured with FLK-TiR32 IR Fusion Themography (Fluke Corporation) within one minute after the uterine horn was exposed to room air.

Mouse brain slice preparation and staining.

Coronal slices of the developing mouse cerebral cortex were prepared as described previously (78). The brains were fixed with 4% paraformaldehyde and cut into 20-40 μm sections with a cryostat. Images of GFP-labeled cells and tdTomato-labeled fibers were captured directly. The primary antibodies used were anti-Brn2 (goat polyclonal, 1:100, Santa Cruz, C-20, sc-6029), anti-PH3 (Ser10, rabbit anti-PH3, 1:200, Millipore, 06-570), anti-nestin (Rat anti-nestin, 1:300, Becton Dickinson, 556309), anti-active-caspase 3 (rabbit anti-active-caspase 3, 1:300, Promega, G748A), anti-NeuN (mouse anti-NeuN, 1:100, Millipore, MAB377), anti-RFP (rabbit anti-RFP, 1:200, Rockland, 600-401-379), and anti-c-Fos (rabbit anti-c-Fos, 1:400, Cell Signaling Technology, 2250S). The nuclei in some sections were labeled with 4', 6-diamidino-2-phenylindole (DAPI, Invitrogen, D3571). Images were acquired through confocal microscopes (FV1000, Olympus Optical) and a fluorescence microscope (BX50, Olympus Optical) equipped with a CCD camera (DP80, Olympus Optical).

Definition of "severely damaged" and "moderately damaged" brains.

By nuclear staining with DAPI, we defined as "severely damaged" when the neocortical CP (cortical plate) was disorganized and showed a cobblestone-like pattern, and as "moderately damaged" when a normal neocortical cytoarchitecture was observed (Supplemental Figure 8).

BrdU labeling.

In vivo BrdU labeling were achieved by intraperitoneally injecting mice with a 50 μg/g body weight dose of BrdU (Sigma). Frozen sections of the brain were prepared

and stained with anti-BrdU antibody (Mouse anti-BrdU, 1:50, Becton Dickinson, 347580).

Quantification of cell distribution.

Cell distribution was statistically analyzed as described previously (79). Briefly, to analyze the distributions of the cells in vivo quantitatively, the nuclei of the GFP-positive cells were visualized by staining with DAPI. First, the relative distance of each cell from the ventricle was determined by measuring the distance (X) of the nucleus from the ventricle with the Image-J software and dividing it (X) by the distance (Y) between the top of the cortical plate and the ventricle along a line that passed through the nucleus (X/Y corresponds to the relative distance of the nucleus from the ventricle). Cell distribution was then evaluated by dividing areas into 5 (Figure 5, E and F) or 10 (Figure 6A and Figure 9, C and D) bins and counting the cells in each bin. The deepest bin was designated Bin 1. For the sake of accuracy, the relative distance of each cell from the ventricle (X/Y above) was used to assign the cells to each of the 5 or 10 bins. For example, in case of 5 bins, cells whose relative distance was >0.8 but $\leqq 1.0$ were assigned to Bin 5, and those whose relative distance was 0 to 0.2 were assigned to Bin 1. The ratio of cells in each bin was calculated by dividing the number of cells in the bin by the total number of cells in all of the bins. In the quantification of cell distribution in the mPFC (Supplemental Figure 9), the relative distance of each cell from the bottom of the cortical plate was determined by measuring the distance (X) of the nucleus from the bottom of the cortical plate with the Image-J software and dividing it (X) by the distance (Y) between the top of the cortical plate and the bottom of the cortical plate along a line that passed through the nucleus (X/Y corresponds to the relative distance of the nucleus from the bottom of the cortical plate).

Other quantification.

Brn2-positive cells in the mouse neocortex in width of 50 μm (Figure 4F), BRN2-positive cells in the human neocortex in width of 50 μm (Figure 4G), PH3-positive cells in the VZ and SVZ in width of 500 μm (Figure 5C and Figure 9B), and BrdU-positive cells and NeuN-positive cells in the WM of the neocortex in width of 1275 μm (Figure 6E) were counted using Image J software.

To analyze contralateral axon branching images from the 40-μm coronal sections

were obtained with a fluorescence microscope (BX50, Olympus Optical) equipped with a CCD camera (DP80, Olympus Optical). The region of interest was defied as a region that included the strongest GFP-expressing contralateral cortical axonal column showing the strongest expression of GFP and had a width greater than 500 μm. The cortical layers within the contralateral cortical axonal columns were identified by DAPI staining. The immunofluorescence in each layer was measured using the Image-J software.

To examine c-Fos expression, c-Fos immunostaining was performed as described previously (34), but using anti-c-Fos antibody (rabbit anti-c-Fos, 1:400, Cell Signaling Technology). To quantify the number of c-Fos-positive cells, we used a confocal microscope (FV1000, Olympus Optical) to scan the slices and calculated the cell numbers from the digitized images of the PrL region in the mPFC using the Image-J software.

Gene microarray analysis.

Neocortex from control or occluded pups at P1.5 was dissected, and total RNA was extracted using AllPrep DNA/RNA/Protein Mini Kit (QIAGEN). RNA was sent to Hokkaido System Science Microarray Team (Hokkaido System Science Co., Ltd.) for cDNA production, labeling and amplification using Low Input Quick Amp Labeling Kit (Agilent Technologies Japan, Ltd.). cDNA was then hybridized to the SurePrint G3 Mouse 8x60k 1 color array (Agilent Technologies Japan, Ltd.) for 17 h at 65°C. Data were analyzed by Agilent Technologies Microarray Scanner and Agilent Feature Extraction 10.7.3.1. The original raw data has been deposited to a public database (NCBI GEO database, the accession number is GSE89998). Analyses of microarray data were performed using the Genespring GX software package (Agilent Technologies Japan, Ltd.). A cutoff at $P < 0.05$ together with a fold cutoff of >1.5 was used to select differentially expressed genes. Significantly changed genes were analyzed for statistically enriched pathways using Ingenuity Pathway Analysis (IPA; Ingenuity Systems).

Open field test.

Mice were placed at the center of an open field (diameter, 60 cm; height, 35 cm) under moderate light conditions (60 lx) and allowed to explore it for 5 min, during which their

activity was measured automatically with the ethovision automated tracking program (Brain Science Idea Co. Ltd.) (80). The open field was divided into an inner circle (diameter, 40 cm) and a surrounding outer area. Mouse movement was measured with a camera mounted above the open field. Measurements included distance traveled and time spent in the inner circle and surrounding outer area.

Locomotor activity test.

The locomotor activity test was carried out as described previously (81). Mice were placed individually in a transparent acrylic cage with a black frosting Plexiglas floor (25×25×20 cm) under moderate light conditions (15 lx), and locomotor activity was measured every 5 min for 120 min by using digital counters and an infrared sensor (Brain Science Idea Co. Ltd.).

Light-dark box test.

The light-dark box test apparatus (O'Hara & Co., Ltd.) consisted of a cage (21 × 42 × 25 cm) divided into two sections of equal size by a partition with a door. The light chamber was brightly illuminated (390 lx), while the dark chamber was dark (2 lx). Mice were placed in the dark chamber and allowed to move freely between the two chambers while the door was open for 10 min. The latency for entering the light chamber was recorded automatically using the Image LD software (O'Hara & Co., Ltd.).

Novel object recognition test.

A novel object recognition test was carried out as described previously (37). Mice were individually habituated to an open box [30 × 30 × 35 (height) cm (Figure 8) or 40 x 40 x 40 (height) cm (Figure 9)] for 3 days. All sessions were conducted under illuminated conditions (16 lx). During the training session two novel objects were placed in the open field, and the animal was allowed to explore for 10 min. The objects used were a golf ball, wooden cylinder, and square pyramid (Figure 8), or were a plastic cap, glass cup, and golf ball (Figure 9), which differed in shape and color but were of similar size. An animal was considered to be exploring the object when its head was facing the object or it was touching or sniffing the object. The time spent exploring each object was recorded by using a video camera, and the data were analyzed in a blinded manner.

In the retention session, the animal was returned to the same box 24 h after the training session, one of the familiar objects used during the training session was replaced by a novel object, and the animal was allowed to explore the two objects freely for 5 min. The exploratory index in the retention session, i.e., the ratio of the amount of time spent exploring the novel object to the total time spent exploring both objects, was used to measure cognitive function. In the training session, a preference index was calculated as the ratio of time spent exploring the object that was replaced by the novel object in the retention session to the total exploration time.

Y-maze test.

Working memory performance was assessed by recording the spontaneous alternation behavior of the animals in the Y-maze test. The maze was made of gray vinyl chloride. Each arm was 40 cm long, 15 cm high, and 3 cm wide at the bottom and 12 cm wide at the top. The arms converged in a triangular central area. The test was conducted as described previously (39, 40). Each mouse, native to the maze, was placed at the end of one arm and allowed to explore the maze freely through the maze for 8 min. Then, the series of arm entries was recorded with a video camera, and the data were analyzed in a blinded manner. A mouse was considered to have entered the arm when its hind paws were placed on the arm. Alternation behavior was defined as successive entries into the three arms, on overlapping triplet sets. The percent of alternations was calculated as the ratio of the actual number (total number of alternations) to the possible number of alternations (total number of arm entries minus two), multiplied by 100.

CNO treatment.

Clozapine-N-oxide (CNO) (Sigma-Aldrich, Co.) was dissolved in DMSO and diluted in saline (0.9% NaCl). In Supplemental Figure 14, the mice in their home cages were intraperitoneally injected with 1 or 5 mg/kg CNO, or control saline (0 mg/kg CNO, 5% DMSO in saline) 2.5 h before the brain fixation. In Figure 8, E-H, the mice expressing hM3Dq in the mPFC were intraperitoneally injected with 1 mg/kg CNO or control saline (0 mg/kg CNO, 5% DMSO in saline) 1 h before the task (Figure 8, E-H) and 3 h before the brain fixation (Figure 8, G and H). In Supplemental Figure 16, the mice expressing hM3Dq in the mPFC were administered control saline by intraperitoneal injection (0 mg/kg CNO, 5% DMSO in saline) 45 min after the start of

the recording, and then with 5 mg/kg CNO by intraperitoneal injection (5 mg/kg CNO, 5% DMSO in saline) 90 min after the start of the recording.

In vivo electrophysiological recording.

Surgical preparation: Mice at 8-10 weeks of age were anesthetized with a mixture ketamine and xylazine (100 mg/kg and 10 mg/kg, respectively, intraperitoneal injection) and fixed to a stereotaxic apparatus (SR-6M, Narishige Scientific Instrument). Their body temperatures were maintained at 37 ± 0.5°C using a heating pad during the surgery. After skull exposure, a U-shaped plastic plate for head fixation was mounted and fixed with a dental acrylic resin (Unifast II, GC Co.) on the head of the mouse. Two small screws were inserted into the occipital bone in contact with the dura for grounding and reference. After covering the exposed skull with the dental acrylic resin, the animal was returned to its home cage for recovery. After recovery from the first surgery (2 or 3 days later), the mouse was anesthetized with sevoflurane (1.5~3%, 0.25 mL/min) and fixed to a stereotaxic apparatus, and a craniotomy was performed to allow insertion of an electrode. The craniotomy (approximately 1 mm in diameter) hole was made 2.0 mm anterior to the bregma and 0.5 mm lateral to the midline on the right, and covered with dental silicone (Dent Silicone-V, Shofu Co.) to protect the underlying brain from drying and infection until the day of the experiment. After the mouse recovered from the second surgery (1 or 2 days later), the awake mouse was positioned in a stereotaxic apparatus using the U-shaped plastic plate. A glass-coated tungsten wire (250 μm diameter, 0.5 MΩ, Alpha Omega) was inserted into the hole to a depth of 1.8 mm. The electrode coated with DiI (D-282, Invitrogen Life Technologies Japan; 80 mg/ml in a 50:50 methanol: acetone mixture) and inserted into the hole to a depth of 1.8 mm.

Extracellular recording and analysis: Recording sessions were started more than 1 h after the insertion of the probes. Local field potentials (LFP) were recorded at 24.42 kHz with a band-pass filter (0.1 Hz–5 kHz) (TDT RZ-2, Tucker-Davis Technologies). The electrophysiological data analysis was performed using the MATLAB software (R2015a, Math Works).

Supplemental Table 1.

Human fetal brain tissue sections from "Hirata collection"

Case	GW	BW	PMI	Sex	Region	Plane	Type of Section
1	19	385g			Frontal	Coronal, Horizontal	Celloidin section
2	23				Frontal	Coronal	Celloidin section
3	23	710g	23h		Frontal	Horizontal	Celloidin section
4	25	780g	5h	M	Frontal	Horizontal	Celloidin section
5	26			M	Frontal	Horizontal	Celloidin section
6	28	1250g		F	Frontal	Coronal	Celloidin section
7	31	1480g	9h	M	Frontal	Horizontal	Celloidin section
8	38	3700g			Frontal	Coronal, Horizontal	Celloidin section
9	23	800g	5h	M	Occipital	Coronal	Cryosection
10	23	633g	3h	M	Occipital	Coronal	Cryosection
11	23	650g	8h	F	Occipital	Coronal	Cryosection
12	25	875g	5h	F	Occipital	Coronal	Cryosection
13	25	900g	4h	F	Occipital	Coronal	Cryosection

Data include the GW (gestational age at death), BW (body weight), PMI (estimated postmortem interval before tissue collection), Sex, Region (used brain regions), Plane (section plane, coronal or horizontal), and Type of section (celloidin-embedded section or cryosection).

Supplemental Table 2.

Comparison cases from archival materials at Texas Children's Hospital.

Case No.	Age	Cortex	Hippocampus	Cerebellum	
1	10 GWs	+			
2	11 GWs	+			
3	14 GWs	+	+	+	
4	15 GWs	+	+	+	
5	15 GWs	+	+	+	
6	18 GWs	+	+	+	
7	19 GWs	+	+	+	
8	20 GWs	+	+	+	
9	21 GWs	+	+	+	
10	22 GWs	+	+	+	
11	22 GWs	+	+	+	
12	22 GWs	+	+	+	
13	23 GWs	+	+	+	
14	23 GWs	+	+	+	
15	23 GWs	+	+	+	
16	23 GWs	+	+	+	
17	24 GWs	+	+	+	
18	26 GWs	+	+	+	Used as a comparison case in Figure 2 and 3A
19	26 GWs	+	+	+	
20	30 GWs	+	+	+	
21	32 GWs	+			
22	34 GWs	+	+	+	
23	37 GWs	+	+	+	
24	38 GWs	+	+	+	
25	38 GWs	+			
26	40 GWs	+	+	+	
27	40 GWs	+			
28	3M	+	+	+	
28	2M	+			
30	9M	+	+	+	
31	22M	+			Used as a comparison case in Figure 3C
32	2Y	+			Used as a comparison case in Supplemental Figure 4A
33	3Y	+			
34	4Y	+			Used as a comparison case in Figure 3C
35	5Y	+			
36	6Y	+			Used as a comparison case in Figure 3B and C
37	9Y	+	+	+	
38	16Y	+			
39	18Y	+	+	+	
40	21Y	+			

A total of 40 brains from the archival materials at Texas Children's Hospital were selected after a careful review of the autopsy histories and descriptions of the microscopic sections. Cases in which white matter lesions were recorded were excluded. However, these cases may have patchy diffuse white matter injuries in other areas of the brain or have subtle white matter changes that require extensive evaluations for visualization, thereby not really serving as "normal" cases. Thus, these brains were mainly used as references to understand developmental stages of the brain in human infants. Plus (+) marks indicate available brain regions as tissue sections. Of these, we also showed five brains as the comparison brains for the histological analyses.

Supplemental Table 3. Summary of the clinical data of the 41 extremely preterm infant cases with white matter injury (WMI).

Case No.	Acute/ Subacute/ Long-term	GW	ST	c-age	Sex	Clinical/Pathological Diagnosis
1	Acute	23	0d	23	M	Potter Syndrome
2	Acute	23	0d	23	F	Arthrogryposis multiplex congenita
3	Acute	23	3d	23	M	Twin, prematurity, Hyaline membrane disease
4	Acute	23	1d	23	M	Respiratory insufficiency, abdominal distention
5	Acute	23	3d	23	M	IVH, bacterial sepsis, RDS, hypotension
6	Acute	24	2d	24	M	Twin, Hyaline membrane disease
7	Acute	25	0d	25	M	GBS infection, Twin
8	Acute	25	1d	25	M	Acute hemorrhage, thrombocytopenia, Twin, Hyaline membrane disease
9	Acute	25	2d	25	M	Coagulopathy
10	Acute	26	0d	26	M	Hypoxic ischemic injury heart & brain, Triplet
11	Acute	26	4d	26	M	Twin-twin transfusion syndrome
12	Acute	26	5d	26	M	Twin-twin transfusion syndrome, RDS, sepsis
13	Acute	26	6d	26	F	RDS
14	Acute	26	6d	26	F	IUGR, Hyaline membrane disease
15	Acute	27	0d	27	M	thoracopagus conjoined twins, CHD
16	Acute	27	0d	27	M	Sepsis, IVH
17	Acute	27	0d	27	F	Triplet, fungal infection
18	Acute	27	1d	27	M	Amniotic fluid infection, Oligohydramnios sequence, CHD
19	Acute	27	3d	27	M	IUGR, Hyaline membrane disease
20	Subacute	23	9d	24	M	Chorioamnionitis, pneumothorax

21	Subacute	23	14d	25	M	Sepsis, pneumothorax
22	Subacute	24	10d	25	F	Intracerebral hemorrhage, Hyaline membrane disease
23	Subacute	24	20d	26	M	Pseudomonas infection
24	Subacute	25	19d	26	M	BPD, NEC
25	Subacute	24	22d	27	M	BPD, NEC, PDA ligation
26	Subacute	25	29d	29	M	NEC, Sepsis
27	Subacute	26	33d	30	M	IUGR, sepsis, tension pneumothorax
28	Subacute	26	42d	32	M	NEC, sepsis, PDA ligation
29	Subacute	26	50d	33	M	NEC
30	Subacute	25	66d	34	M	NEC
31	Long-term	25	4m	0.25m	F	RDS, sepsis, triplet
32	Long-term	26	4m	0.5m	M	RDS, NEC, PDA ligation, Chronic neonatal lung disease, sepsis, respiratory failure with prolonged mechanical ventilation, Twin
33	Long-term	24	5m	1m	M	Infection
34	Long-term	25	5m	1.25m	F	Sepsis, myocardial infarction, triplet, Chronic neonatal lung disease, hypothyroidism
35	Long-term	24	6m	2m	M	Twin, multiple abdominal surgeries of NEC, Bacterial infection, life long mechanical ventilation
36	Long-term	26	6m	2.5m	M	Twin, NEC, BPD
37	Long-term	27	1y	8.75m	M	CP, PVL, shock
38	Long-term	23	21m	16.75 m	M	NEC, short gut syndrome, Chronic neonatal lung disease
39	Long-term	25	18m	14.25 m	F	Chronic neonatal lung disease, NEC, Twin, RDS
40	Long-term	24	2y	20m	M	Neonatal meningitis, CP, MR, static encephalopathy
41	Long-term	24	6y	68m	M	BPD, seizure, CP

Data include the type of case (Acute: 0-6 days/Subacute: 9-66 days/Long-term: 4 months to 6 years), GW (gestational age at birth), ST (survival time after birth), c-age (corrected age at the time of death, weeks in the Acute and Subacute cases or months [m] after 40 GWs in the Long-term cases), sex, and clinical/pathological diagnosis.
RDS: respiratory distress syndrome, GBS: Group B Streptococcus, NEC: necrotizing enterocolitis, IUGR: intrauterine growth retardation, CHD: congenital heart disease, IVH: intraventricular hemorrhage, BPD: bronchopulmonary dysplasia, PDA: patent ductus arteriosus, CP: cerebral palsy, PVL: periventricular leukomalacia, MR: mental retardation

Supplemental Table 4.

The characteristic morphologic features of WMI were evaluated in the white matter of 41 autopsy extremely preterm infant brains.

	Number (percent)		
	Acute cases	Subacute cases	Long-term cases
total number	19	11	11
coagulation necrosis	6 (32)	9 (82)	1 (9.1)
microglia infiltration	19 (100)	11 (100)	11 (100)
axonal swelling	6 (32)	7 (64)	9 (82)
astrocyte proliferation	10 (53)	10 (91)	11 (100)
foam cell	6 (32)	5 (45)	9 (82)
calcification	1 (5.2)	2 (18)	5 (45)
dying cells	18 (95)	9 (82)	3 (27)
cyst formation	0 (0)	2 (18)	2 (18)

As previously reported (7), the white matter lesions were non-focal and diffusely distributed throughout the white matter, but a volumetric evaluation was impossible because of the specimen limitation. Cyst formation, a pathologic landmark of classic PVL, was observed in only 4 cases. Representative images of a case with cyst formation are shown in Supplemental Figure 4. All of the acute cases (n = 19, average birth at 25.2 ± 1.6 GWs, duration of survival 1.9 ± 2.1 days, corrected age at death 25.2 ± 1.6 GWs) exhibited increased numbers of microglial cells, and dying cells were observed in 95% of the acute cases. Most of the subacute cases (n = 11, average birth at 24.6 ± 1.1 GWs, duration of survival 28.4 ± 17.9 days, corrected age at death 28.3 ± 3.5 GWs) exhibited microglial proliferation, axonal swelling, and astrocytosis. All long-term cases (n = 11, average birth at 24.8 ± 1.2 GWs, duration of survival 16.1 ± 19.9 months, corrected age at death 12.3 ± 19.8 months) exhibited increased numbers of microglia and reactive astrocytes. Foam cells (histiocytes) were frequently observed in the long-term cases. In all the extremely preterm infant cases with WMI the white matter lesions were characterized by diffuse and immature necrotic changes with increased numbers of microglia and astrocytes.

Supplemental Table 5.

Disruption of the VZ/SVZ/ependymal epithelium in extremely preterm infants with WMI and the presence/absence of intraventricular hemorrhage (IVH).

Case No	Acute/ Sucacute/ Long-term	Measured length of ventricular surface (μm)	Percentage of disruption	Presence(+) or Absence (-) of IVH
1	Acute	15596	18.39%	-
2	Acute	15687	20.08%	+
3	Acute	24695	58.92%	+
4	Acute	19080	29.65%	+
5	Acute	26940	72.28%	+
6	Acute	14649	51.96%	+
7	Acute	21620	16.31%	+
8	Acute	15438	47.56%	+
9	Acute	8739	82.44%	+
10	Acute	16754	31.52%	-
11	Acute	14743	16.93%	+
12	Acute	16701	38.72%	-
13	Acute	31595	77.43%	+
14	Acute	21322	76.01%	+
15	Acute	12876	12.12%	-
16	Acute	9022	20.27%	+
17	Acute	24278	47.15%	+
18	Acute	38568	84.47%	-
19	Acute	18174	27.08%	+
20	Subacute	12980	44.13%	+
21	Subacute	20201	49.23%	-
22	Subacute	13725	49.98%	+
23	Subacute	22367	70.29%	+
24	Subacute	14146	33.51%	+
25	Subacute	15443	54.15%	+
26	Subacute	11502	47.29%	-
27	Subacute	31831	9.62%	-
28	Subacute	35608	100.00%	+
29	Subacute	13065	42.89%	-
30	Subacute	23940	43.69%	+
31	Long-term	19180	83.54%	
32	Long-term	7807	87.50%	
33	Long-term	11872	82.99%	+
34	Long-term	14207	41.47%	
35	Long-term	7140	94.05%	+
36	Long-term	7502	79.98%	+
37	Long-term	17022	70.17%	-
38	Long-term	12199	95.70%	
39	Long-term	4399	76.12%	
40	Long-term	47578	91.53%	+
41	Long-term	18635	97.08%	-

To measure the degree of disruption of the ventricular zone (VZ)/subventricular zone (SVZ)/ependymal epithelium in extremely preterm infants with WMI, we measured the ratio of the ventricular surface showing disrupted cellular disorganization by dividing the length of the ventricular surface showing disrupted cellular disorganization by the total length of the ventricular surface in each section.

The duration of survival was partly correlated with the extent of the lesions; acute and subacute cases tended to present with partial (focal) lesions, whereas long-term survivors had more extensive (widespread to complete) lesions (Supplementary Figure 4C).

Supplemental Table 6.

Blood-gas analyses data.

	Control (n = 3)	Occluded (n = 4)
pH	7.313 ± 0.013	6.971 ± 0.034
$PaCO_2$ (mmHg)	37.1 ± 3.9	68.1 ± 10.2
PaO_2 (mmHg)	82.7 ± 7.0	47.3 ± 4.1
BE (mmol/L)	-7.3 ± 2.2	16.3 ± 1.6
SaO_2 (%)	95 ± 1.5	56.8 ± 7.6

Blood samples were collected from the uterine arteries of dams in the control group (Control) and the occluded group (Occluded). Means ± S.E. of blood-gas analysis data are shown.

Supplemental Table 7.

Microarray gene expression analysis of control versus occluded brains from mouse pups at P1.

ProbeName	FC ([Occluded] vs [Control])	FC (abs) ([Occluded] vs [Control])	Regulation ([Occluded] vs [Control])	GeneSymbol	EntrezGeneID	GeneName
A_55_P2005475	3.7865996	3.7865996	up	Sult1a1	20887	sulfotransferase family 1A, phenol-preferring, member 1
A_51_P256827	3.7012823	3.7012823	up	S100a8	20201	S100 calcium binding protein A8 (calgranulin A)
A_55_P2269819	3.3631954	3.3631954	up	Fam107a	268709	family with sequence similarity 107, member A
A_51_P321341	3.348934	3.348934	up	Sult1a1	20887	sulfotransferase family 1A, phenol-preferring, member 1
A_51_P509573	-3.148907	3.148907	down	Ccl4	20303	chemokine (C-C motif) ligand 4
A_51_P167292	3.1191921	3.1191921	up	Chil3	12655	chitinase-like 3
A_52_P507214	-2.9049335	2.9049335	down	Mmp9	17395	matrix metallopeptidase 9
A_55_P1963154	2.867865	2.867865	up	Folh1	53320	folate hydrolase 1
A_55_P2015541	2.856905	2.856905	up	Hif3a	53417	hypoxia inducible factor 3, alpha subunit
A_55_P1998471	2.7766004	2.7766004	up	S100a9	20202	S100 calcium binding protein A9 (calgranulin B)
A_51_P381618	2.7030358	2.7030358	up	Pla1a	85031	phospholipase A1 member A
A_51_P140710	-2.5804858	2.5804858	down	Ccl3	20302	chemokine (C-C motif) ligand 3
A_51_P265495	2.2644572	2.2644572	up	Ly6a	110454	lymphocyte antigen 6 complex, locus A
A_51_P411345	-2.1858144	2.1858144	down	Mogat2	233549	monoacylglycerol O-acyltransferase 2
A_55_P2152364	-2.149678	2.149678	down	Runx2os1	100038355	runt related transcription factor 2, opposite strand 1
A_51_P335569	2.1330056	2.1330056	up	Slco1a4	28250	solute carrier organic anion transporter family, member 1a4
A_52_P680751	2.12709	2.12709	up	Cux1	13047	cut-like homeobox 1
A_51_P185660	-2.0876887	2.0876887	down	Ccl9	20308	chemokine (C-C motif) ligand 9
A_30_P01028902	-2.0796466	2.0796466	down			
A_55_P1961499	2.0675395	2.0675395	up	Ly6c1	17067	lymphocyte antigen 6 complex, locus C1
A_52_P64763	-2.0279548	2.0279548	down	Gen1	209334	Gen homolog 1, endonuclease (Drosophila)
A_55_P2109033	1.9916008	1.9916008	up	Hmgcs2	15360	3-hydroxy-3-methylglutaryl-Coenzyme A synthase 2
A_51_P241995	1.944063	1.944063	up	Col5a3	53867	collagen, type V, alpha 3
A_66_P139546	1.9306703	1.9306703	up	Igfbp6	16012	insulin-like growth factor binding protein 6
A_55_P2185372	1.9084626	1.9084626	up	Sirt4	75387	sirtuin 4
A_55_P2021981	-1.8969502	1.8969502	down	Ctsw	13041	cathepsin W
A_30_P01018027	-1.8920132	1.8920132	down			
A_30_P01027214	-1.8913376	1.8913376	down			
A_55_P2103190	-1.8789464	1.8789464	down			
A_52_P151227	-1.8685192	1.8685192	down	LOC102638165	102638165	uncharacterized LOC102638165
A_55_P2364738	-1.8572079	1.8572079	down	Plxdc1	72324	plexin domain containing 1
A_30_P01019455	-1.8547968	1.8547968	down			
A_55_P2148403	-1.8498558	1.8498558	down			
A_51_P421140	-1.8049215	1.8049215	down	Tubb6	67951	tubulin, beta 6 class V
A_55_P2154709	-1.7986627	1.7986627	down	Pter	19212	phosphotriesterase related
A_52_P796840	1.7963213	1.7963213	up	Cfhr2	545366	complement factor H-related 2
A_55_P2064771	1.7928647	1.7928647	up	Ly6c1	17067	lymphocyte antigen 6 complex, locus C1
A_51_P362066	-1.7905496	1.7905496	down	Chil1	12654	chitinase-like 1
A_30_P01024091	-1.7758662	1.7758662	down			
A_30_P01029553	-1.771854	1.771854	down			
A_30_P01024622	-1.7615677	1.7615677	down			
A_51_P460954	-1.7500229	1.7500229	down	Ccl6	20305	chemokine (C-C motif) ligand 6
A_52_P515826	-1.7494599	1.7494599	down	Med13	327987	mediator complex subunit 13
A_55_P1988048	1.7458267	1.7458267	up	Emcn	59308	endomucin
A_55_P2111302	1.7383515	1.7383515	up	Cp	12870	ceruloplasmin
A_55_P2168346	-1.7371057	1.7371057	down	Banf2	403171	barrier to autointegration factor 2
A_66_P132249	-1.7223352	1.7223352	down	Akr1c13	27384	aldo-keto reductase family 1, member C13
A_30_P01029871	-1.7140328	1.7140328	down			
A_55_P2010271	-1.708752	1.708752	down	Samsn1	67742	SAM domain, SH3 domain and nuclear localization signals, 1
A_55_P1962747	-1.7076668	1.7076668	down	H2-Ab1	14961	histocompatibility 2, class II antigen A, beta 1
A_51_P519791	-1.7007089	1.7007089	down	Ska3	219114	spindle and kinetochore associated complex subunit 3
A_55_P2167763	-1.6960955	1.6960955	down			
A_30_P01022894	1.6953809	1.6953809	up			
A_30_P01020117	-1.6887254	1.6887254	down			
A_30_P01029735	-1.687263	1.687263	down			
A_55_P2025746	-1.6865903	1.6865903	down	Adam5	11499	a disintegrin and metallopeptidase domain 5
A_55_P1973326	-1.6813668	1.6813668	down			

A_55_P2017418	1.679301	1.679301	up	Cfh	12628	complement component factor h
A_55_P2077048	1.6783977	1.6783977	up	Itih5	209378	inter-alpha (globulin) inhibitor H5
A_55_P2010641	-1.6771201	1.6771201	down	Slc38a5	209837	solute carrier family 38, member 5
A_55_P2037081	-1.6757469	1.6757469	down	2610305D13Rik	112422	RIKEN cDNA 2610305D13 gene
A_55_P2124554	-1.675037	1.675037	down	Cep41	83922	centrosomal protein 41
A_51_P442964	-1.673774	1.673774	down	Casc5	76464	cancer susceptibility candidate 5
A_51_P470328	1.6713656	1.6713656	up	Sepp1	20363	selenoprotein P, plasma, 1
A_55_P2071191	-1.6712885	1.6712885	down	Prss8	76560	protease, serine 8 (prostasin)
A_30_P01021490	-1.6672086	1.6672086	down			
A_51_P501656	-1.6655803	1.6655803	down	Kdelc2	68304	KDEL (Lys-Asp-Glu-Leu) containing 2
A_30_P01026797	-1.6539584	1.6539584	down			
A_55_P1989673	1.6532056	1.6532056	up	Slco2a1	24059	solute carrier organic anion transporter family, member 2a1
A_51_P487555	-1.6505077	1.6505077	down	Cd7	12516	CD7 antigen
A_55_P2088615	1.6462609	1.6462609	up	Fbln5	23876	fibulin 5
A_55_P2146560	-1.6458315	1.6458315	down	H2-Ab1	14961	histocompatibility 2, class II antigen A, beta 1
A_51_P324529	-1.643283	1.643283	down	Calcoco2	76815	calcium binding and coiled-coil domain 2
A_51_P366138	1.6336652	1.6336652	up	Mertk	17289	c-mer proto-oncogene tyrosine kinase
A_55_P2127995	-1.6324984	1.6324984	down	Ccl19	24047	chemokine (C-C motif) ligand 19
A_30_P01020116	1.6280141	1.6280141	up			
A_55_P2019569	-1.6217383	1.6217383	down	Vmn2r62	546964	vomeronasal 2, receptor 62
A_55_P2454521	-1.6193459	1.6193459	down	Alms1	236266	Alstrom syndrome 1
A_55_P2166618	-1.6174163	1.6174163	down			
A_55_P1960068	-1.6085893	1.6085893	down			
A_30_P01020074	-1.6068298	1.6068298	down			
A_30_P01028039	-1.606638	1.606638	down			
A_52_P499206	-1.6058679	1.6058679	down	Tbl2	27368	transducin (beta)-like 2
A_52_P444517	-1.6044884	1.6044884	down	Pfn3	75477	profilin 3
A_52_P375323	-1.5987568	1.5987568	down	Slc9a9	331004	solute carrier family 9 (sodium/hydrogen exchanger), member 9
A_30_P01025131	-1.5930482	1.5930482	down			
A_55_P2351193	-1.5899084	1.5899084	down	Snora47	100217450	small nucleolar RNA, H/ACA box 47
A_52_P552879	1.5895041	1.5895041	up	Efcab4a	213573	EF-hand calcium binding domain 4A
A_55_P2118491	-1.5867773	1.5867773	down	Gm10046	100043229	predicted gene 10046
A_55_P2162573	-1.5850457	1.5850457	down	Art3	109979	ADP-ribosyltransferase 3
A_55_P2003211	-1.5823858	1.5823858	down	Igsf5	72058	immunoglobulin superfamily, member 5
A_55_P2040594	-1.5804291	1.5804291	down	Pabpc5	93728	poly(A) binding protein, cytoplasmic 5
A_30_P01023646	-1.5794541	1.5794541	down			
A_30_P01032346	1.5783886	1.5783886	up			
A_51_P256665	-1.5762386	1.5762386	down	Pon3	269823	paraoxonase 3
A_30_P01029877	-1.5761591	1.5761591	down			
A_66_P121171	-1.5682977	1.5682977	down	Gm15413	791381	predicted gene 15413
A_55_P2207255	-1.5640924	1.5640924	down	Srpx	51795	sushi-repeat-containing protein
A_55_P2022724	-1.5547458	1.5547458	down	5430417L22Rik	100043272	RIKEN cDNA 5430417L22 gene
A_30_P01020417	-1.5539745	1.5539745	down			
A_55_P1956687	-1.5524298	1.5524298	down	Rab37	58222	RAB37, member RAS oncogene family
A_30_P01022882	-1.5510331	1.5510331	down			
A_55_P1961720	1.5477471	1.5477471	up	Kcnt1	227632	potassium channel, subfamily T, member 1
A_55_P1974804	1.5465877	1.5465877	up	Slc24a4	238384	solute carrier family 24 (sodium/potassium/calcium exchanger), m4
A_55_P2065231	1.5462939	1.5462939	up	Gstm3	14864	glutathione S-transferase, mu 3
A_51_P208769	-1.54525	1.54525	down	Metrn	70083	meteorin, glial cell differentiation regulator
A_55_P2100834	-1.545087	1.545087	down	Sprtn	244666	SprT-like N-terminal domain
A_30_P01024138	1.5449986	1.5449986	up			
A_52_P123693	-1.5448201	1.5448201	down	E130304I02Rik	78547	RIKEN cDNA E130304I02 gene
A_55_P2031781	-1.5434688	1.5434688	down	Col22a1	69700	collagen, type XXII, alpha 1
A_55_P2044932	-1.5419604	1.5419604	down	Gpr84	80910	G protein-coupled receptor 84
A_55_P1985850	-1.5401303	1.5401303	down	Timp1	21857	tissue inhibitor of metalloproteinase 1
A_55_P2064506	1.5390536	1.5390536	up	Defb36	266620	defensin beta 36
A_55_P2152427	-1.536692	1.536692	down	Zwilch	68014	zwilch kinetochore protein
A_55_P2056496	-1.5344027	1.5344027	down	Tk1	21877	thymidine kinase 1
A_55_P1966432	1.5335442	1.5335442	up	Gstm1	14862	glutathione S-transferase, mu 1
A_55_P2108324	1.5315245	1.5315245	up	Med12	59024	mediator complex subunit 12
A_30_P01022325	-1.5306766	1.5306766	down			
A_55_P2472435	-1.5285258	1.5285258	down	Gbp3	55932	guanylate binding protein 3
A_30_P01027130	-1.5283144	1.5283144	down			
A_30_P01028703	1.5273446	1.5273446	up			
A_30_P01022304	-1.526883	1.526883	down			
A_55_P2174987	-1.5264616	1.5264616	down	Creb3l3	208677	cAMP responsive element binding protein 3-like 3
A_51_P419286	-1.5263007	1.5263007	down	Batf3	381319	basic leucine zipper transcription factor, ATF-like 3
A_30_P01022991	-1.5248466	1.5248466	down			

A_55_P2020326	−1.5187333	1.5187333	down	Madcam1	17123	mucosal vascular addressin cell adhesion molecule 1
A_66_P101835	1.518158	1.518158	up	Cd38	12494	CD38 antigen
A_55_P2052265	−1.5176955	1.5176955	down	Zscan30	328918	zinc finger and SCAN domain containing 30
A_30_P01030189	1.5154725	1.5154725	up			
A_55_P1954216	−1.5153148	1.5153148	down	Ugt3a1	105887	UDP glycosyltransferases 3 family, polypeptide A1
A_52_P600946	1.5152528	1.5152528	up	Ccdc88c	68339	coiled-coil domain containing 88C
A_51_P240723	−1.5146525	1.5146525	down	1700022A21Rik	72252	glycerol-3-phosphate dehydrogenase 1-like pseudogene
A_30_P01030106	−1.5142156	1.5142156	down			
A_51_P150678	1.5108002	1.5108002	up	Tnfaip8l2	69769	tumor necrosis factor, alpha-induced protein 8-like 2
A_55_P2123291	−1.5106169	1.5106169	down	2310034G01Rik	75579	RIKEN cDNA 2310034G01 gene
A_30_P01019353	−1.5104078	1.5104078	down			
A_30_P01033446	−1.50941	1.50941	down			
A_55_P2154027	−1.5084141	1.5084141	down	Ptgis	19223	prostaglandin I2 (prostacyclin) synthase
A_51_P159503	−1.508324	1.508324	down	Rnf213	672511	ring finger protein 213
A_52_P227279	−1.5057812	1.5057812	down	Vipr1	22354	vasoactive intestinal peptide receptor 1
A_30_P01023511	−1.5007789	1.5007789	down			

Microarray analysis was performed using the SurePrint G3 Mouse 8x60k 1 color array (Agilent Technologies). $N = 4$ mice, per group. Up-regulated probes/genes in occluded brains are shown in shades of red and down-regulated probes/genes in occluded brains are shown in shades of blue. The original raw data has been deposited to a public database (NCBI GEO database, the accession number is GSE89998).

Supplemental Figure 1

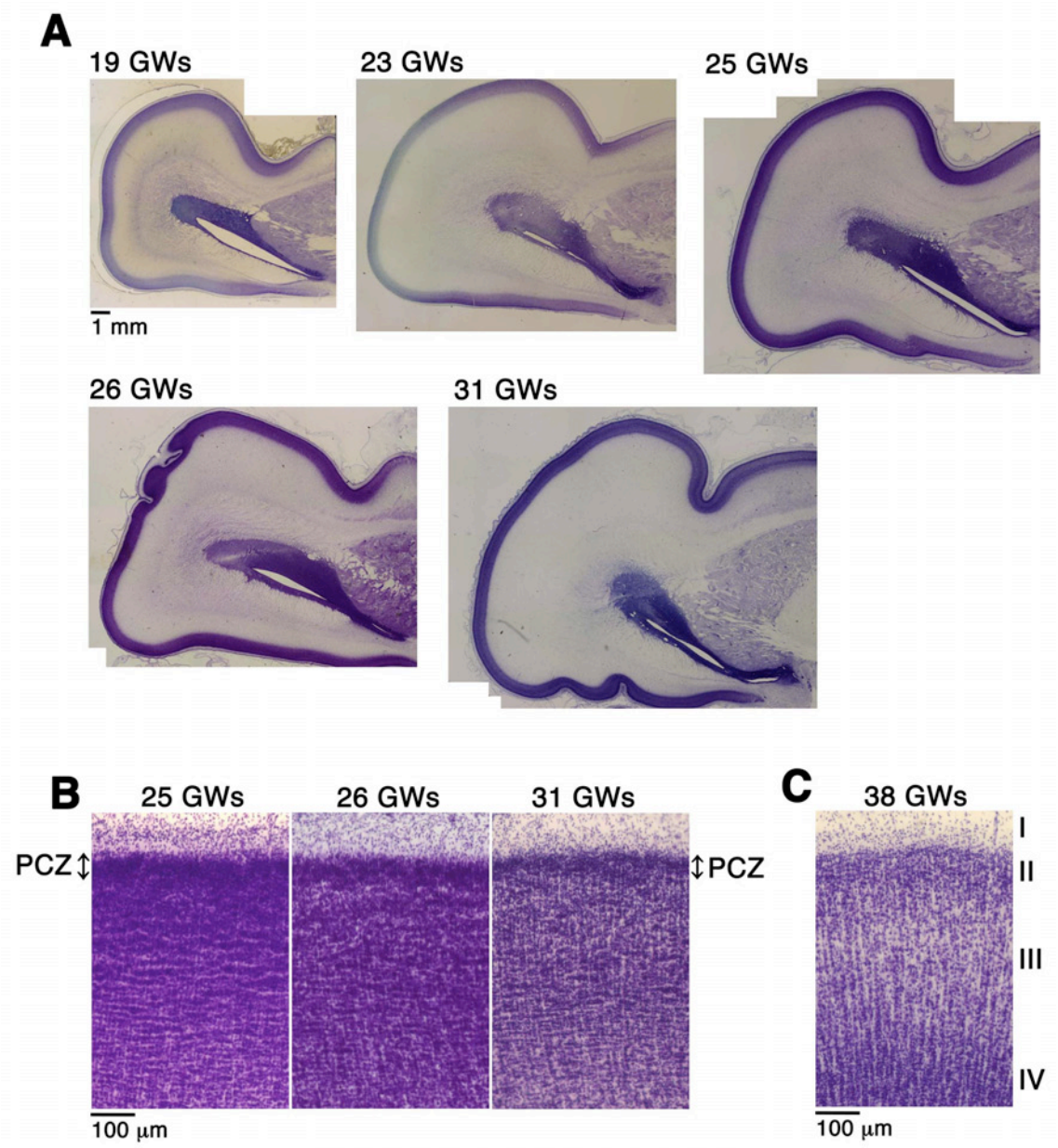

Supplemental Figure 1.

Analyses of horizontal sections of the human neocortices.

(**A**) Horizontal sections of the human neocortices at 19, 23, 25, 26 and 31 GWs were stained with Cresyl violet (Nissl staining). Higher magnifications of the areas around the ventricles are shown in Figure 1, (**E**).

(**B**) Higher magnifications of the forming cortical plate (CP) in (**A**). The outermost regions of the neocortices at 25, 26 and 31 GWs showing cell-dense accumulation of

neurons. This region is thought to correspond to the primitive cortical zone (PCZ).
(**C**) The PCZ-like structure is not observed and distinct cortical layers are apparent in horizontally sliced sections from a brain at 38 GWs.

Supplemental Figure 2

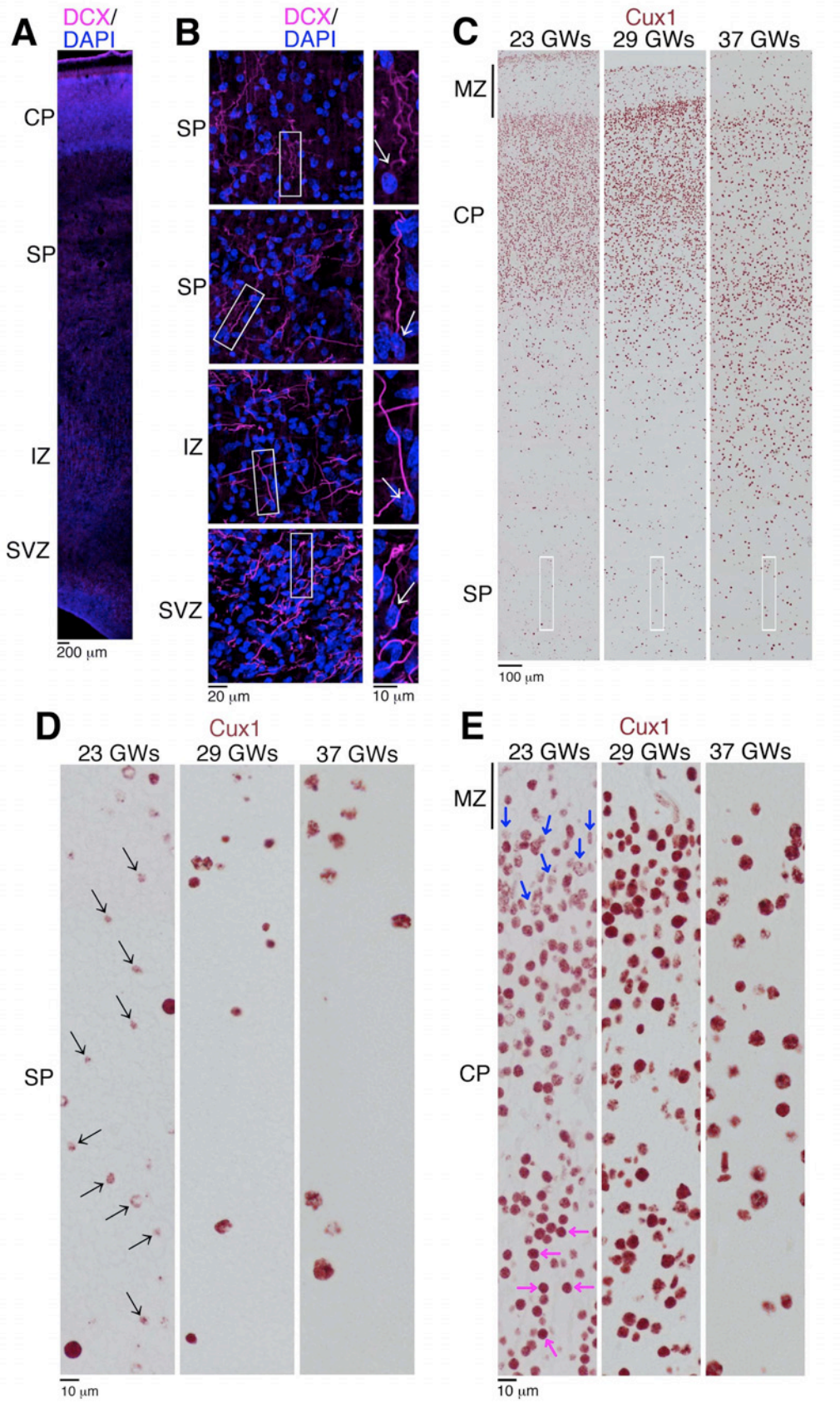

Supplemental Figure 2.

Analyses of human neocortices.

(**A**) A section of the human neocortex at 25 GWs was immunostained with anti-doublecortin (DCX) antibody (magenta) and counterstained with DAPI (blue). CP, cortical plate. SP, subplate. IZ, intermediate zone. SVZ, subventricular zone. (**B**) Higher magnifications of (**A**) are shown in the panels on the left. Further higher magnifications of the boxed areas in (**B**) are shown in the panels on the right. DCX-positive cells showed the characteristic features of migrating neurons with long leading processes (indicated by arrows).

(**C**-**E**) Sections from the human temporal neocortex at 23, 29 and 37 GWs stained with anti-CUX1 (CUTL1) antibody. Higher magnifications of the boxed areas in (**C**) are shown in (**D**). Cells that were moderately positive for CUX1 were diffusely distributed throughout the neocortex, including the SP (indicated by arrows in **D**), at 23 GWs.

(**E**) Higher magnifications of the top of the neocortex in (**C**). At 23 GWs, most cells beneath the MZ (marginal zone) were moderately positive for CUX1 (blue arrows, for example), whereas in the deeper part of the cortical plate, the cells tended to be strongly positive for CUX1 (magenta arrows, for example), suggesting that the cells that were moderately positive for CUX1 were migrating or had just completed migration, and that those that were strongly positive for CUX1 were more mature. Cells that were strongly positive for CUX1 were more sparsely distributed at the top of the neocortex at 37 GWs than at 23 GWs or 29 GWs, suggesting disappearance of the PCZ-like structure at 37 GWs.

Supplemental Figure 3

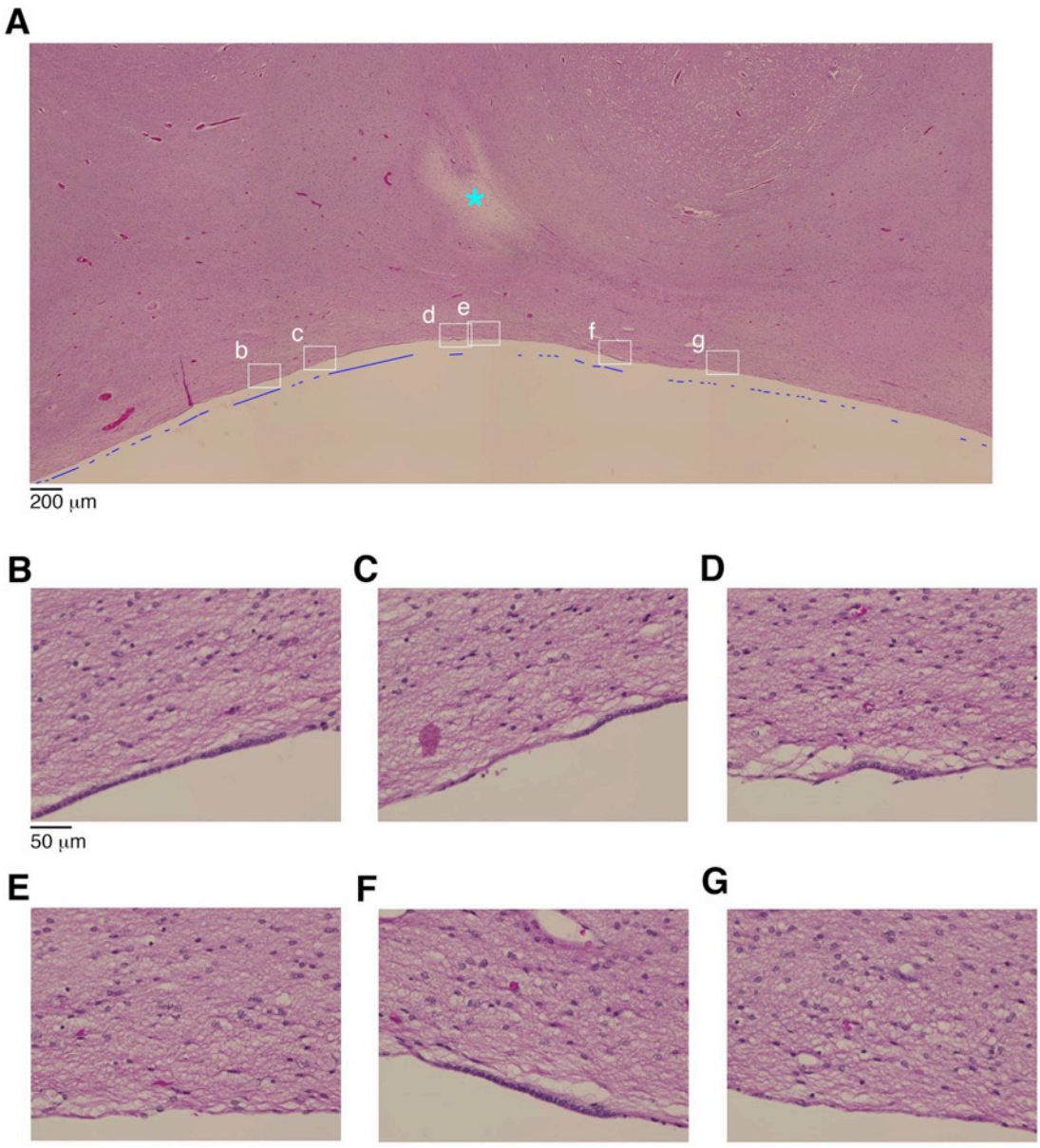

Supplemental Figure 3.

An example of a loss of continuity of ependymal epithelium in a long-term survival case.

(**A**) Histological appearance of the human neocortex facing the ventricle from a long-term survivor's brain (27 GWs at birth, survived 1 year) with WMI is shown. Serial sections were stained with HE. Although cyst formation, a pathologic landmark of classic PVL, was observed in only 4 cases in our study (Supplemental Table 4), faint cyst formation was observed in this case (indicated by a cyan asterisk). The cellular

organization of the ependyma was disrupted focally, even in distant regions from the focal cyst formation (the remaining ependymal regions are shown by blue lines).
(**B**-**G**) Higher magnifications of (b)-(g) in (**A**) are shown. In (**B**) and (**F**), the cellular organization of the ependyma was largely maintained. In (**E**) and (**G**), the ependyma was mostly lost. In (**C**) and (**D**), disrupted and maintained ependymal regions were admixed.

Supplemental Figure 4

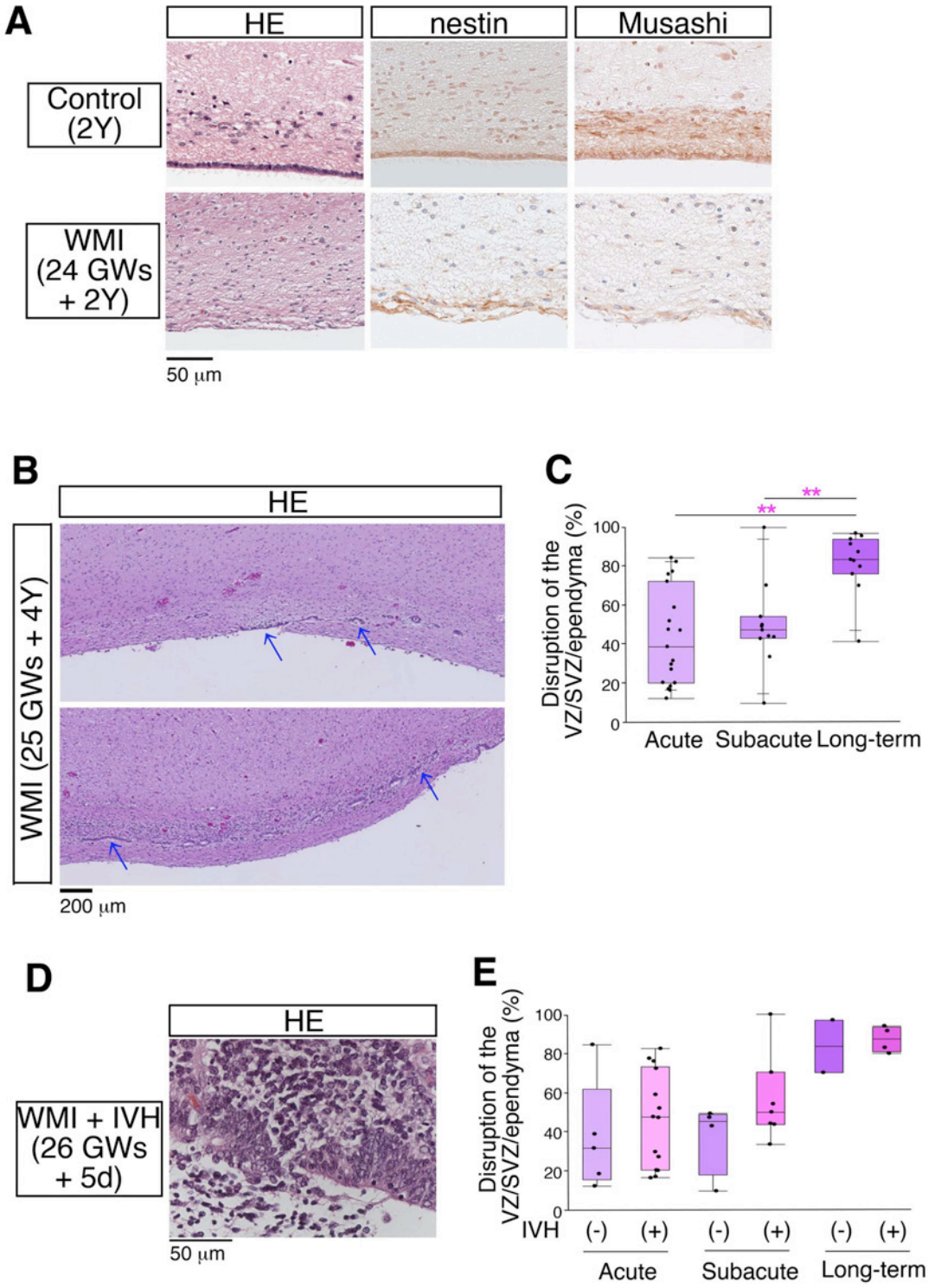

Supplemental Figure 4.

Histological analyses of neocortical ventricular surfaces from extremely preterm infants.

(**A**) Histological appearance of the human neocortex facing the ventricle from a comparison brain (at 2 years) and a long-term survivor's brain (24 GWs at birth, survived 2 years) with WMI is shown. Serial sections were stained with HE and immunostained with anti-nestin and Musashi1 antibodies. The cellular organization of the ependymal epithelium was disrupted in this long-term survivor's brain with WMI (bottom panels).

(**B**) Histological appearance of the human neocortex facing the ventricle from a long-term survivor's brain (25 GWs at birth, survived 4 year) with WMI is shown. Serial sections were stained with HE. The cellular organization at the ventricular surface was largely disrupted, with relatively little intact ependymal epithelium (indicated by blue arrows).

(**C**) To examine the degree of disruption of the VZ/SVZ/ependymal epithelium in extremely preterm infants with WMI, we have quantitatively measured the ratio of the disrupted ventricular surface by dividing the length of the ventricular surface with disrupted cellular disorganization by the total length of the ventricular surface in each section. Graph indicates degree of disruption of the ventricular surface in each survivor (Acute: $n = 19$, Subacute: $n = 11$, Long-term: $n = 11$). $^{**}P < 0.01$, $^{***}P < 0.001$, Tukey-Kramer test.

(**D**) Histological appearance of the SVZ/VZ of the neocortex from an extremely preterm infant with WMI (26 GWs at birth, survived 5 days) with intraventricular hemorrhage (IVH). The VZ and SVZ lesions were extensive in this case.

(**E**) The degree of disruption was not significantly different between the brains of the survivors with and without IVH (Acute: $P = 0.509$, Student's *t*-test, absence (-): $n = 5$, presence (+): $n = 14$, Subacute: $P = 0.179$, Student's *t*-test, absence (-): $n = 4$, presence (+): $n = 7$, Long-term: P value was not calculated because of the small sample size, absence (-): $n = 2$, presence (+): $n = 4$).

(**C** and **E**) Each point represents an individual brain. Box-and-whisker plots were used to graphically represent the median (line within box), upper and lower quartiles (bounds of box), and maximum and minimum values (top and bottom bars).

Supplemental Figure 5

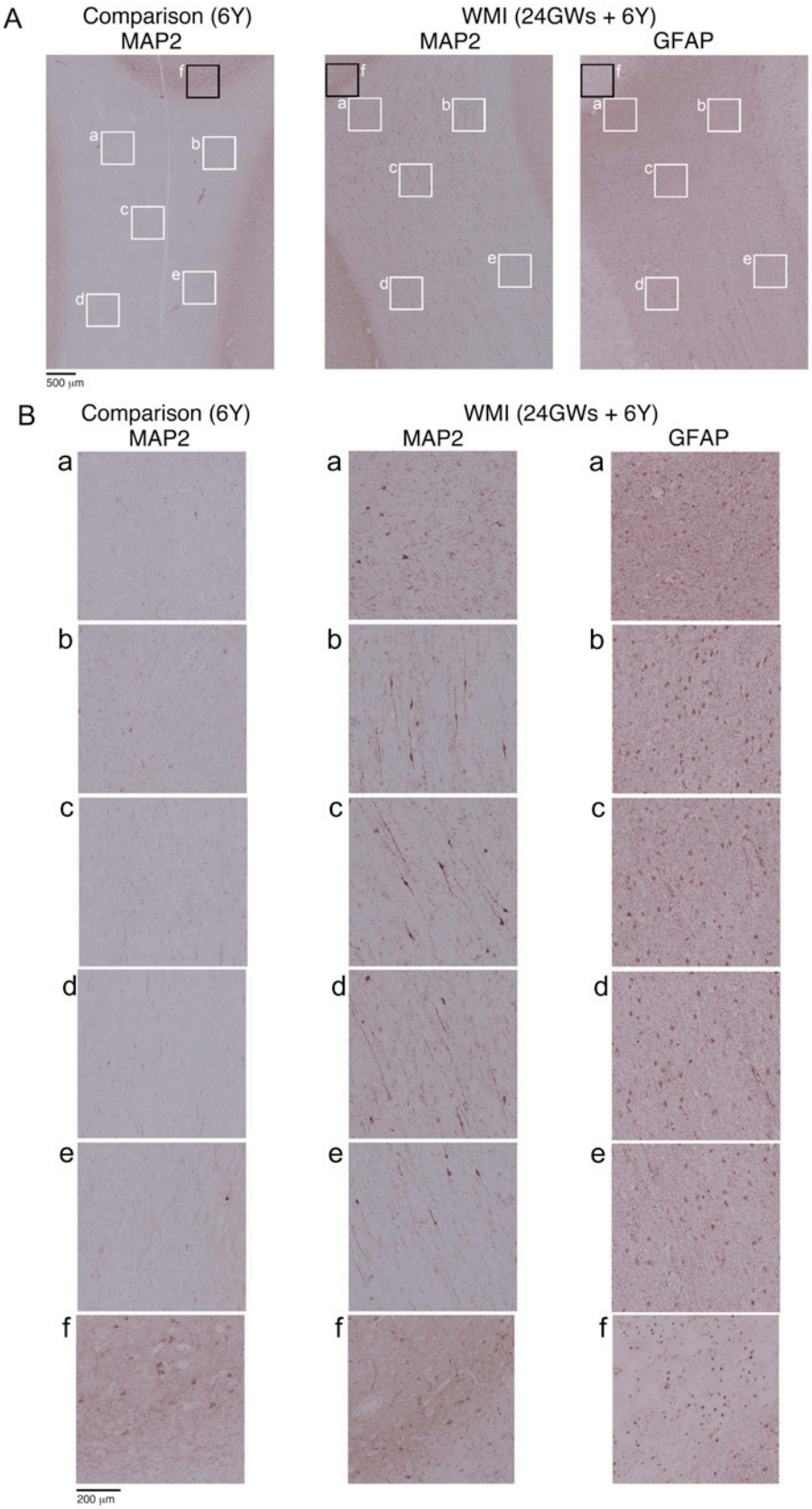

Supplemental Figure 5.

Histological analyses of the white matters.

(**A** and **B**) Sections of neocortex of a comparison case (6-year old) and a long-term survivor (24 GWs at birth, survived 6 years) with WMI were immunostained for MAP2 and GFAP. Higher magnifications of the boxed areas of white matter (a-e) and gray matter (f) are shown in (**B**).

Supplemental Figure 6

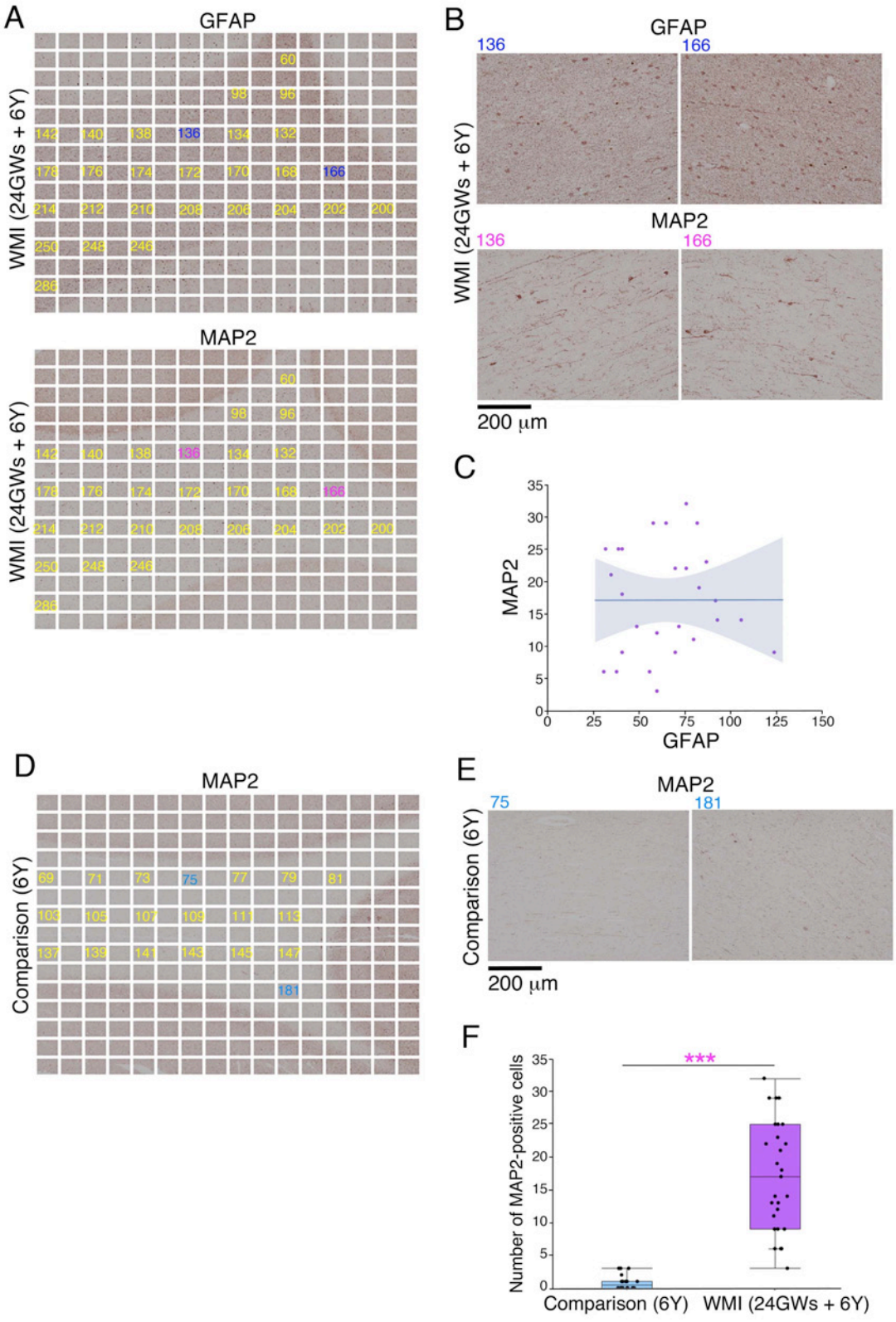

Supplemental Figure 6.

Investigation of local variations of the Map2- and GFPA-positive cells in the white matter.

(**A**) Nearby sections of the neocortex of a long-term survivor (24 GWs at birth, survived 6 years) with WMI were immunostained for MAP2 and GFAP. Tile-scan images of high-power fields (x20) were acquired through a microscope (BZ-X700, Keyence) and images were selected to cover the white matter and avoid overwrap, and assigned numbers. Images of corresponding sections were assigned the same number.

(**B**) Higher-magnifications of the images assigned the numbers 136 and 166 in (**A**) are shown, for example.

(**C**) The numbers of MAP2- and GFAP-positive cells in each image were counted and plotted. The correlation between the number of MAP2-positive cells and the number of GFAP-positive cells was poor, with a correlation coefficient $r = 0.00169$ ($n = 27$, $P = 0.993$), indicating that the number of MAP2-positive cells was not significantly correlated with the number of GFAP-positive cells. The line was calculated by the method of least squares. Blue shading indicates the 95% confidence intervals.

(**D**) A section of the neocortex of a comparison case (6-year old) was immunostained for MAP2. Tile-scan images of high-power fields (x20) were acquired through a microscope (BZ-X700, Keyence) and images were selected to cover the white matter and avoid overwrap, and assigned numbers.

(**E**) Higher magnifications of the images assigned the number 75 and 181 in (**D**) are shown, for example.

(**F**) MAP2-positive cells in the white matter were quantified by counting the number of cells in the number-assigned images of (**A**) (WMI, a long-term survivor with WMI) and (**D**) (Comparison). The numbers of MAP2- positive cells per field are shown (Comparison: $n = 20$ fields, WMI: $n = 27$ fields). ***$P < 0.001$, Welch's t-test.

(**C** and **F**) Each point represents an individual field. Box-and-whisker plots were used to graphically represent the median (line within box), upper and lower quartiles (bounds of box), and maximum and minimum values (top and bottom bars).

Supplemental Figure 7

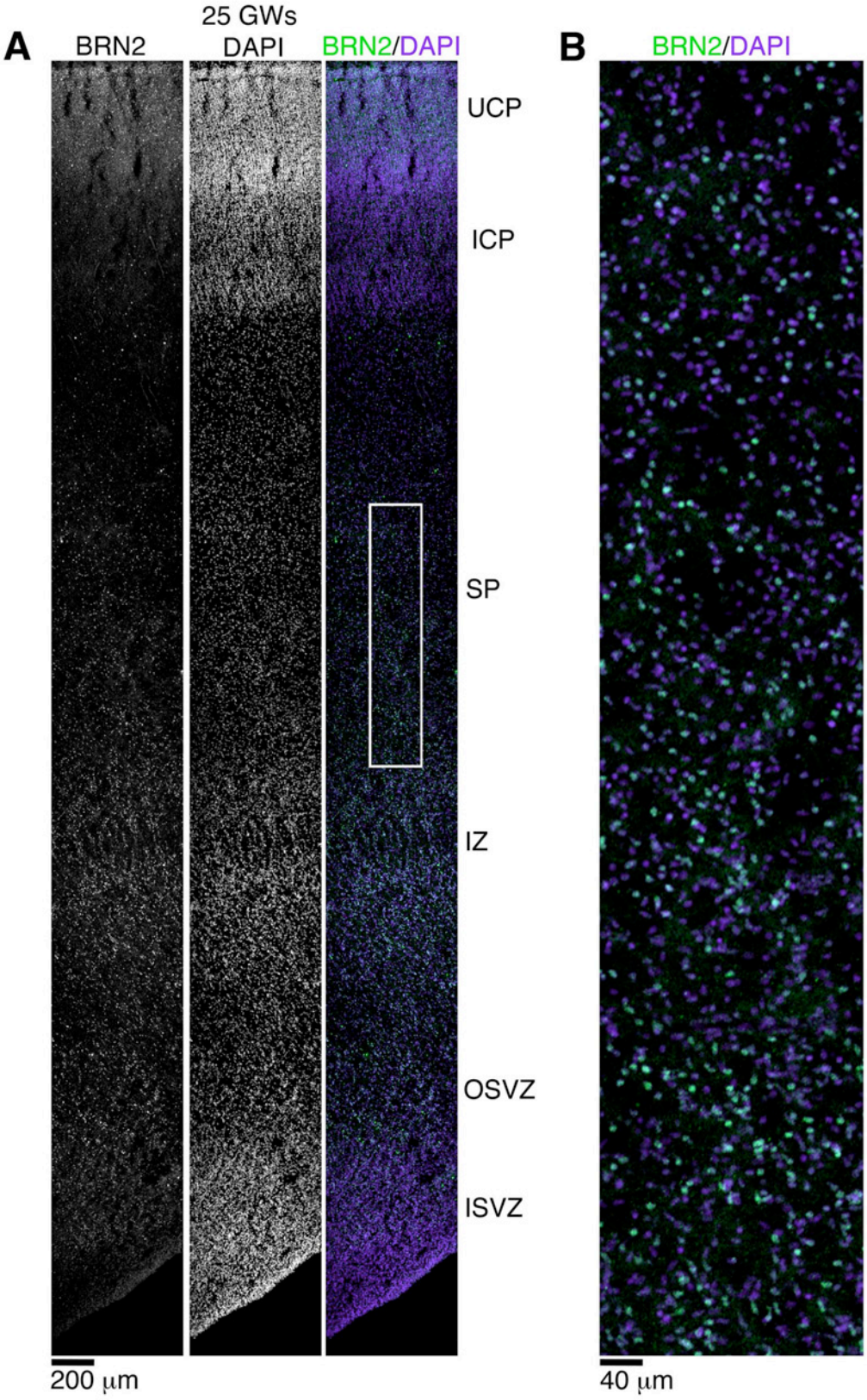

Supplemental Figure 7.

BRN2-positive cells were abundantly distributed in the SP and IZ of the human neocortex at 25 GWs.

(**A** and **B**) Sections from the human occipital neocortex at 25 GWs were stained with anti-BRN2 antibody (green). Sections were counterstained with DAPI (purple). Higher magnification of the boxed area in (**A**) is shown in (**B**). Cells that were positive for BRN2 (green) were abundantly distributed throughout the neocortex, including the subplate (SP) and intermediate zone (IZ). UCP, upper cortical plate. LCP, lower cortical plate. OSVZ, outer subventricular zone. ISVZ, inner subventricular zone.

Supplemental Figure 8

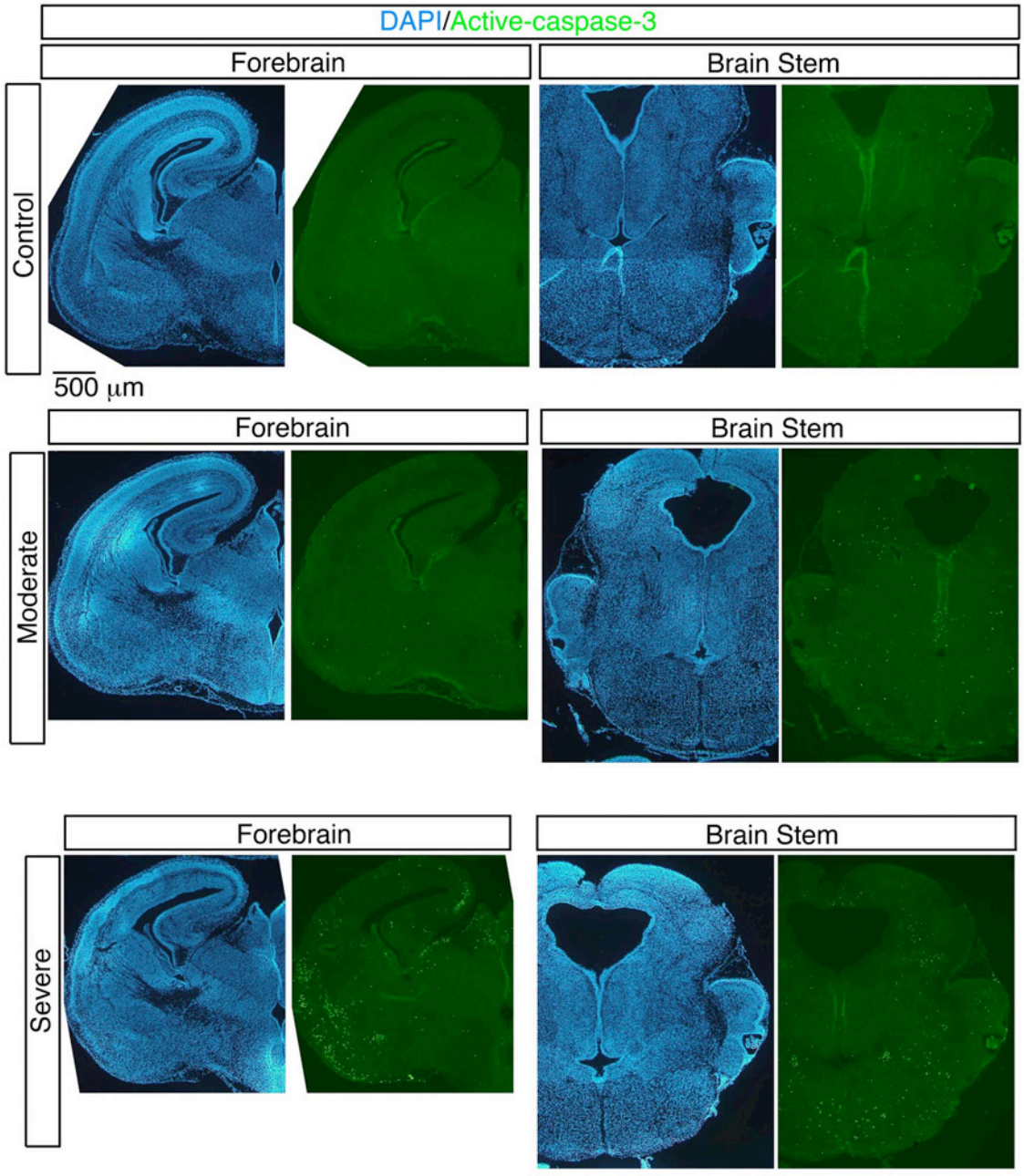

Supplemental Figure 8.

Active caspase-3-positive signals in control brains and occluded brains.

Brains of control embryos (top panels) and occluded embryos (middle and bottom panels) were analyzed 12 h after maternal uterine artery occlusion. Sections of neocortices were immunostained with an anti-active-caspase-3 antibody and counterstained with DAPI. Sections of forebrain and brain stem from the same brains

are shown. By nuclear staining with DAPI, the brain was defined as “severely damaged” when the neocortical cortical plate was disorganized and showed a cobblestone-like pattern (Severe, bottom panels), and as “moderately damaged” when a normal neocortical cytoarchitecture was observed (Moderate, middle panels).

Even when brain deformities were severe (Severe, bottom panels), neocortical structures generally stained negative or minimally positive for active-caspase-3. However, some other brain regions contained scattered active-caspase-3-positive cells. The active-caspase-3-positive areas in the severely damaged brains included the piriform cortex, central gray matter of the midbrain, reticular formation, locus ceruleus, and Purkinje cells in the cerebellum (bottom panels). This extensive brain damage was assumed to underlie the failure of the severely damaged embryos to survive and result in the smaller litter size. In contrast, there were few active-caspase-3-positive signals in the moderately damaged brains, in which neocortical structures appeared to have remained normal (middle panels).

Supplemental Figure 9

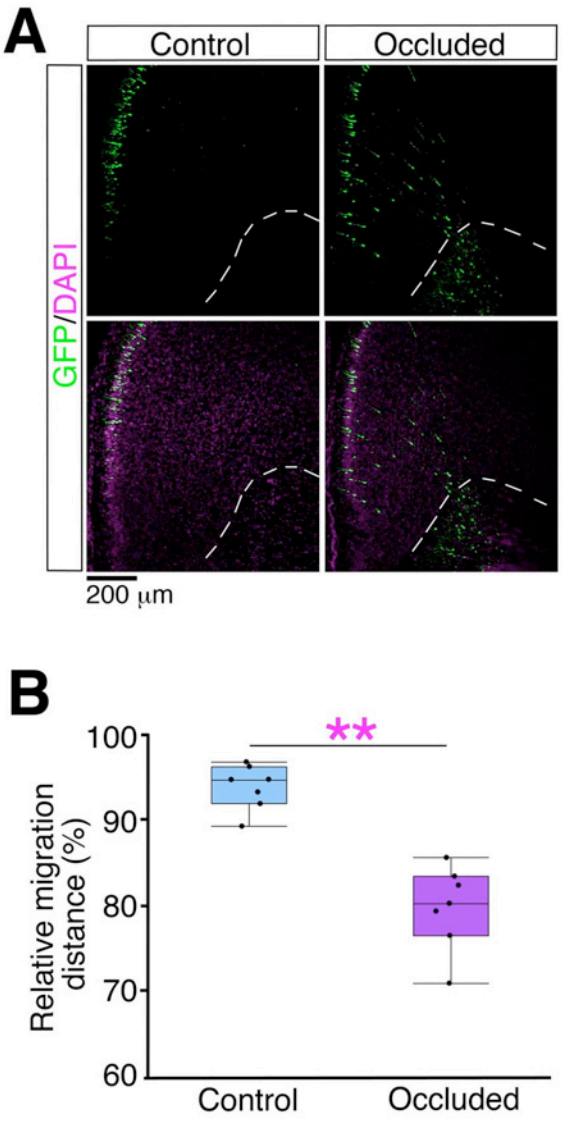

Supplemental Figure 9.

Migration defects were also observed in the medial prefrontal cortex (mPFC).

(**A**) After transfection of GFP expression plasmid at E15.0, a sham operation (control) or maternal uterine artery occlusion (occluded) was performed at E16.5. The mPFC regions of brains were analyzed at P1 (counterstained with DAPI, magenta). Broken lines indicate the bottom lines of the gray matter corresponding to the boundaries of the gray and white matter.

(**B**) Relative migration distances (%) from the bottom lines of cortical plate (gray matters). Means ± S.E. of average relative migration distances are shown (n = 7, respectively). $^{**}P < 0.01$, Student's t-test.

Supplemental Figure 10

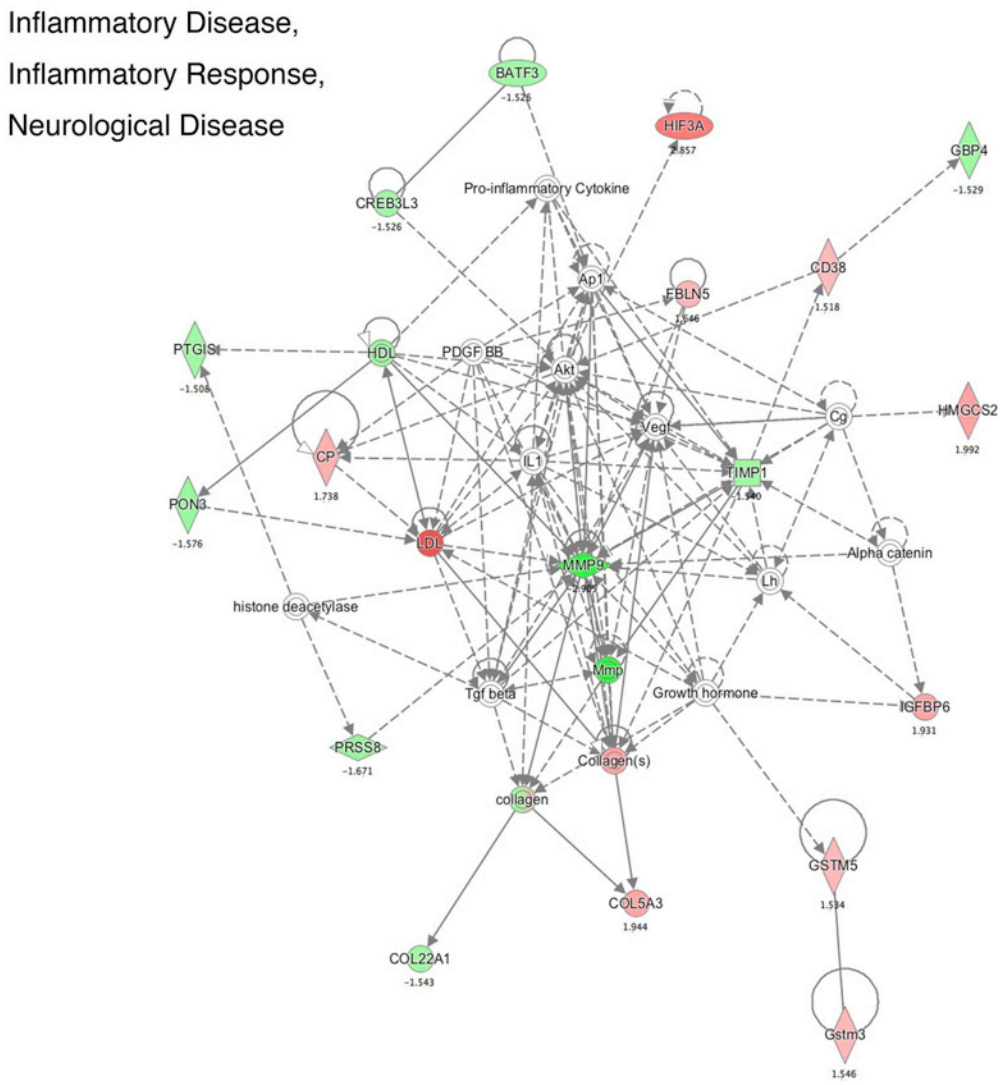

Supplemental Figure 10.

Associated network analysis of the enriched genes.

Associated network analysis was performed using the IPA software based on differentially expressed genes between the neocortices of the control and occluded mice (n = 4, respectively, Supplementary Table 7). "Inflammatory Disease, Inflammatory Response, Neurological Disease" was detected as the top associated network function by IPA. Red and green nodes represent the up- and downregulated genes, respectively.

Supplemental Figure 11

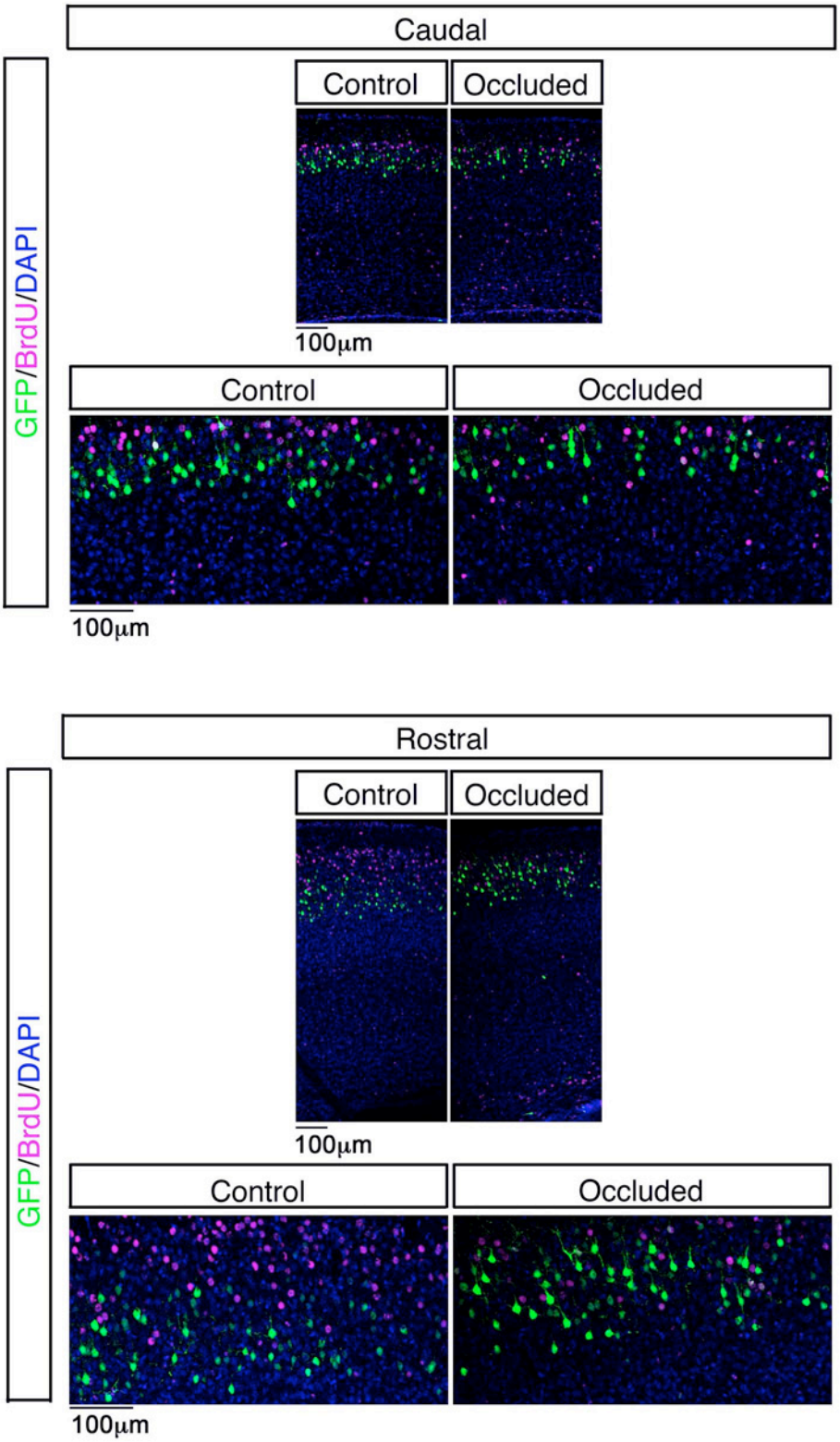

Supplemental Figure 11.

The maternal uterine artery occlusion resulted in abnormal neuronal alignment throughout the neocortex.

Coronal sections from caudal or rostral parts of brains are shown. After transfecting a GFP expression plasmid at E15.0, we performed a sham operation (control group) or maternal uterine artery occlusion (occluded group) at E16.5 and injected BrdU at E17.0. Brains were analyzed at P10, 14 days after electroporation. Sections of neocortices were immunostained with anti-BrdU antibody (magenta) and counterstained with DAPI (blue). Each lower panel shows a higher magnification of the superficial area of the neocortex. The distributions of BrdU-positive cells were intermingled with the distributions of the GFP-positive cells in the ischemic brains, indicating disruption of the “inside-out” neuronal alignment.

Supplemental Figure 12

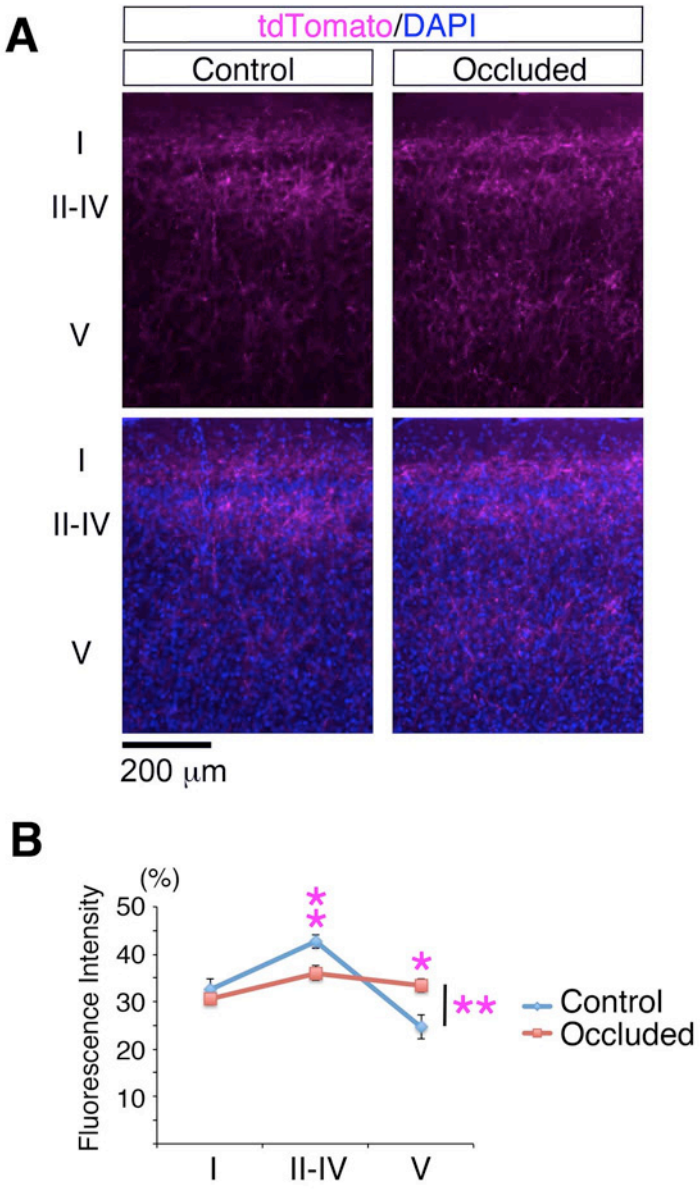

Supplemental Figure 12.

Aberrant axonal branching was observed in the mPFC of the ischemic mice at P15. (**A**) Contralateral axonal branching of the GFP-positive cells in the opposite hemisphere in the mPFC of P15 mice that had been transfected with a GFP expression plasmid in the developing mPFC at E15.0. In the control brains (Control), the GFP-labeled axons branched extensively in the superficial layers (I and II/III). However, in the occluded brains (Occluded), extensive axonal branching was also observed in the deeper layer (layers V).

(**B**) Fluorescence intensity of GFP in each layer was quantified to analyze axonal branching. The GFP intensity was significantly reduced in layer II/III and increased in layer V in the occluded brains (n = 7) compared to the control brains (n = 8). Means ± S.E. of relative fluorescence intensity are shown. *P < 0.05, **P < 0.01, repeated measures ANOVA followed by Bonferroni post-hoc test.

Supplemental Figure 13

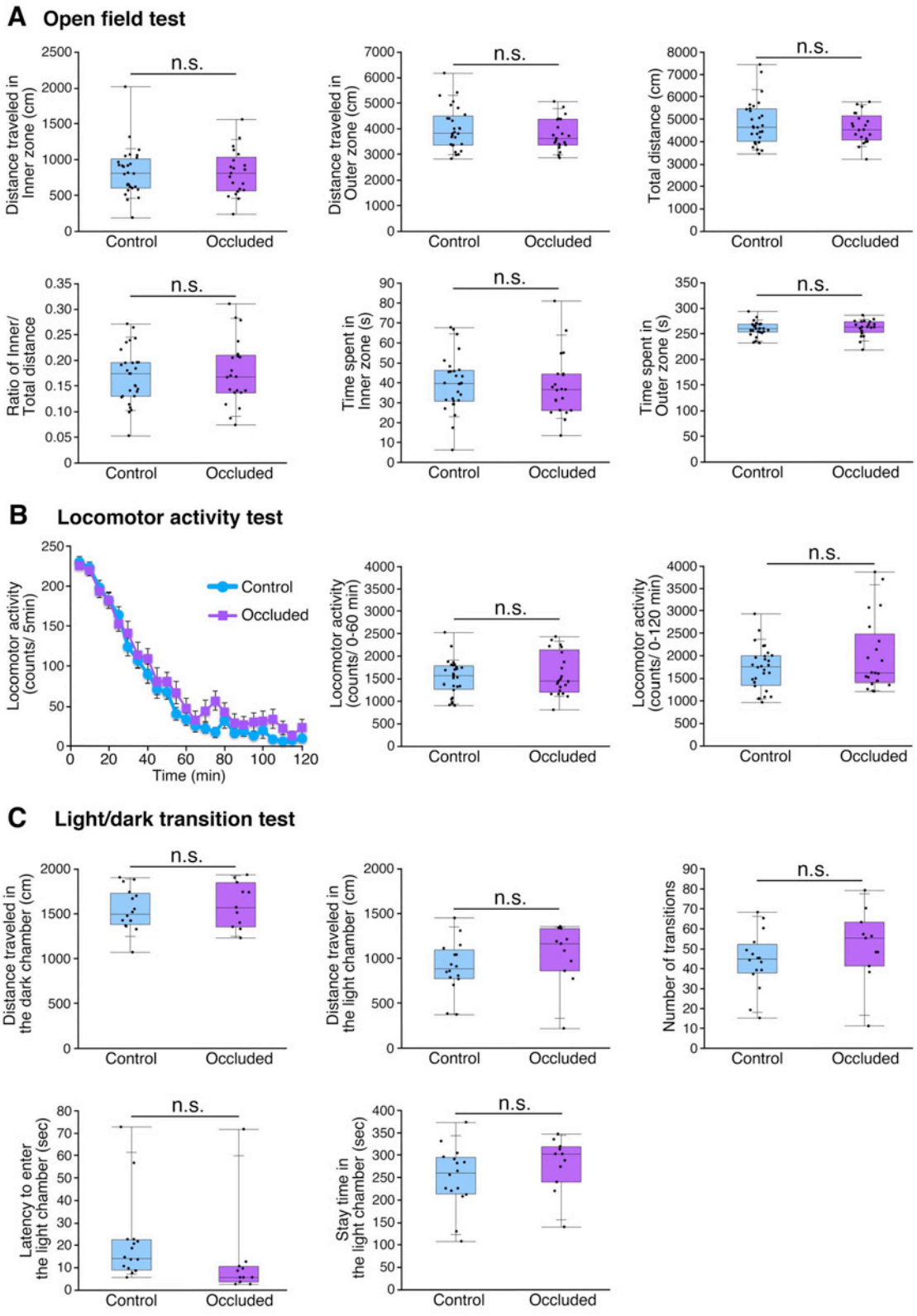

Supplemental Figure 13.

Effect of the maternal uterine artery occlusion on the behavioral performance of mice.

(**A**) Individual mice were allowed to freely explore the open field for 5 min. Distance traveled in inner zone, distance traveled in outer zone, total distance traveled, travel distance ratio of the inner sectors, time spent in inner zone, and time spent in outer zone are shown (n = 28 for control group, n = 21 for occluded group). There were no significant differences between the occluded group and control group in time spent and distance traveled in each zone (distance traveled in inner zone: P = 0.888, Student's t-test, distance traveled in outer zone: P = 0.274, Student's t-test, time spent in inner zone: P = 0.782, Student's t-test, and time spent in outer zone: P = 0.724, Student's t-test), nor did the maternal uterine artery occlusion have any effect on the total distance traveled in the open field (P = 0.322, Student's t-test) or the ratio of inner distance traveled to total distance traveled (P = 0.686, Student's t-test).

(**B**) Changes in locomotor activity during a 120-min period are shown in the left panel. Total locomotor activity during the first 60 min and during the total 120-min period is shown in right panel. Values are means ± S.E. (n = 28 for control group, n = 21 for occluded group). No significant differences were observed between the two groups (0-60 min: P = 0.513, Student's t-test, 0-120 min: P = 0.153, Student's t-test).

(**C**) Mice were placed into a dark chamber and allowed to move freely between the dark and light chambers while the door was kept open for 10 min. The distance traveled in the dark chamber, distance traveled in the light chamber, number of transitions, latency to enter the light chamber, and the stay time in the light chamber are shown (n = 16 for control group, n = 11 for occluded group). There were no significant differences in the time spent in the light chamber and distance traveled in either chamber between the occluded group and control group (stay time in the light chamber: P = 0.264, Student's t-test, distance traveled in the dark chamber: P = 0.575, Student's t-test, and distance traveled in the light chamber: P = 0.254, Student's t-test), nor did the maternal uterine artery occlusion have any effect on the number of transitions (P = 0.223, Student's t-test) or latency to enter the light chamber (P = 0.299, Student's t-test).

(**A**-**C**) Each point represents an individual mouse. Box-and-whisker plots were used to graphically represent the median (line within box), upper and lower quartiles (bounds of box), and maximum and minimum values (top and bottom bars).

Supplemental Figure 14

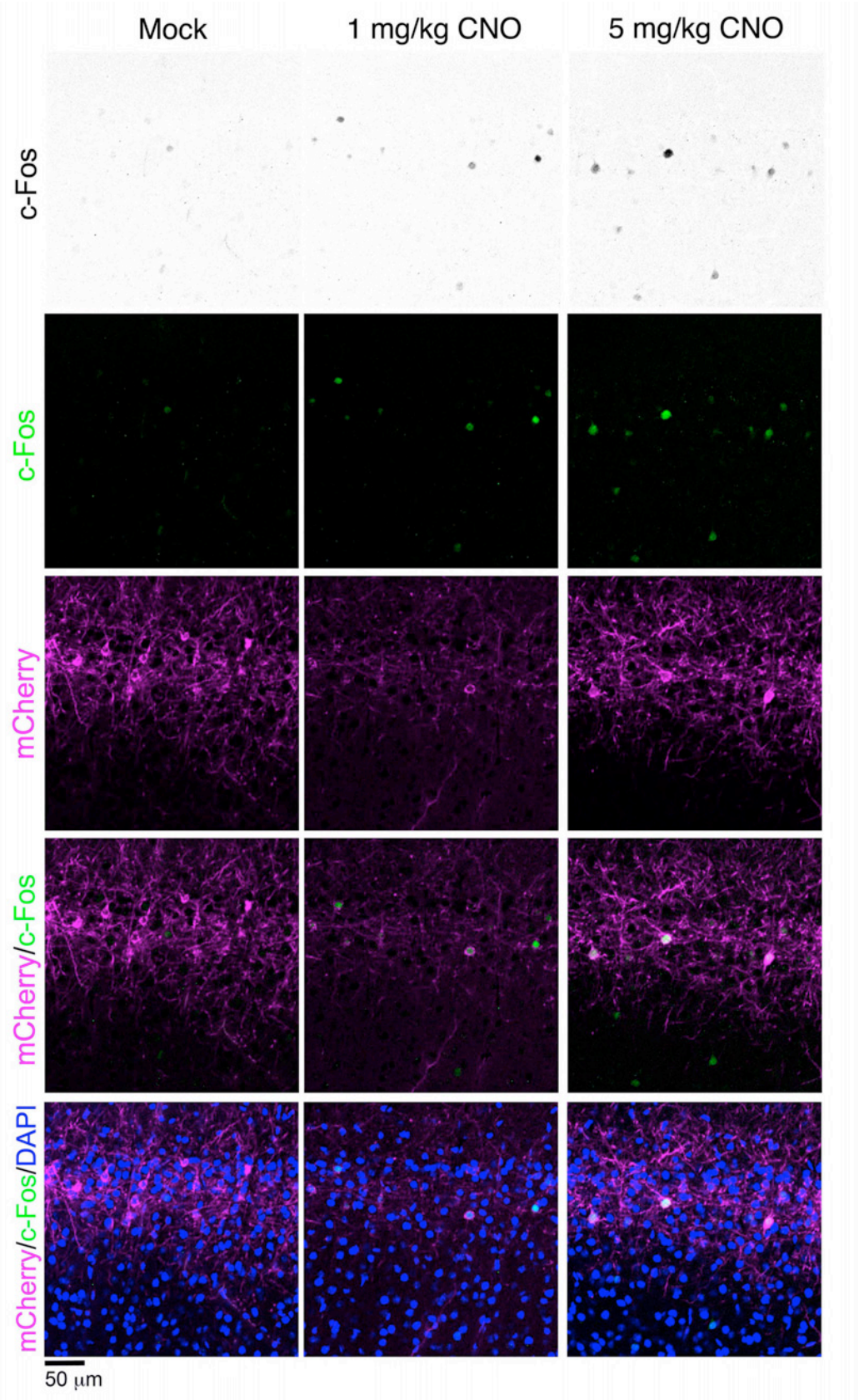

Supplemental Figure 14.

Injection of CNO induced elevation of c-Fos expression in the hM3Dq-mCherry introduced cells.

An hM3Dq-expressing vector (pCAG-hM3Dq-mCherry) was electroporated with pCAG-EGFP into the right and left mPFC of mice at E15.0 by *in utero* electroporation. The mice at P4W in their home cages were intraperitoneally injected with 1 or 5 mg/kg of CNO or control saline (0 mg/kg CNO, 5% DMSO in saline) 2.5 h before brain fixation. An marked of c-Fos expression was markedly observed especially in the mCherry-positive-cells, in the presence of 1 or 5 mg/kg CNO, but not in the absence of CNO (0 mg/kg CNO), indicating that the injected CNO induced excitation of the hM3Dq-mCherry-transfected neurons.

Supplemental Figure 15

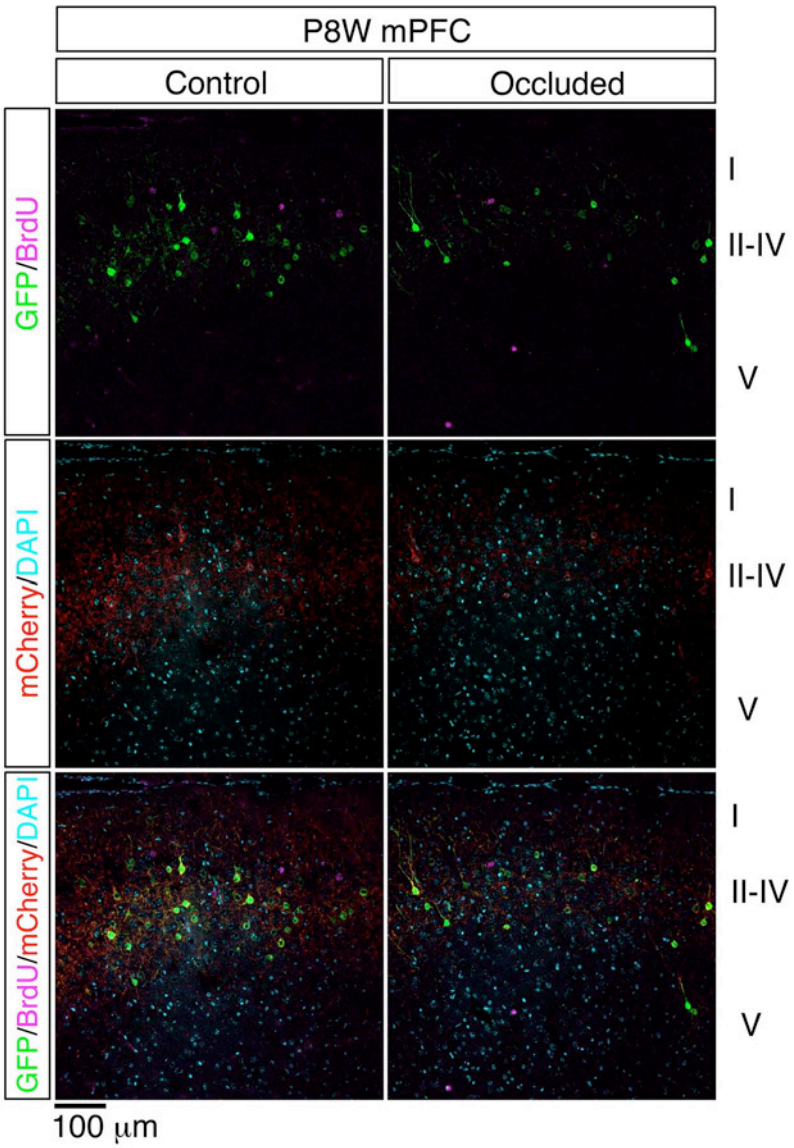

Supplemental Figure 15.

The maternal uterine artery occlusion resulted in abnormal neuronal alignment in the mPFC.

Coronal sections from the mPFC of P8W mice brains are shown. After transfecting a GFP expression plasmid and an hM3Dq-expressing vector (pCAG-hM3Dq-mCherry) at E15.0, we performed a sham operation (control group) or maternal uterine artery occlusion (occluded group) at E16.5 and injected BrdU at E17.0. Brains were analyzed at P8W. Sections were immunostained with anti-RFP (red) and anti-BrdU antibodies

(magenta) and counterstained with DAPI (cyan). In the occluded brains, ectopic BrdU- or GFP-positive cells were observed but most of the GFP-positive cells tended to be distributed in more superficial positions compared with the control mice. The distributions of BrdU-positive cells were intermingled with the distributions of the GFP-positive cells in the occluded brains, indicating disruption of the “inside-out” neuronal alignment.

Supplemental Figure 16

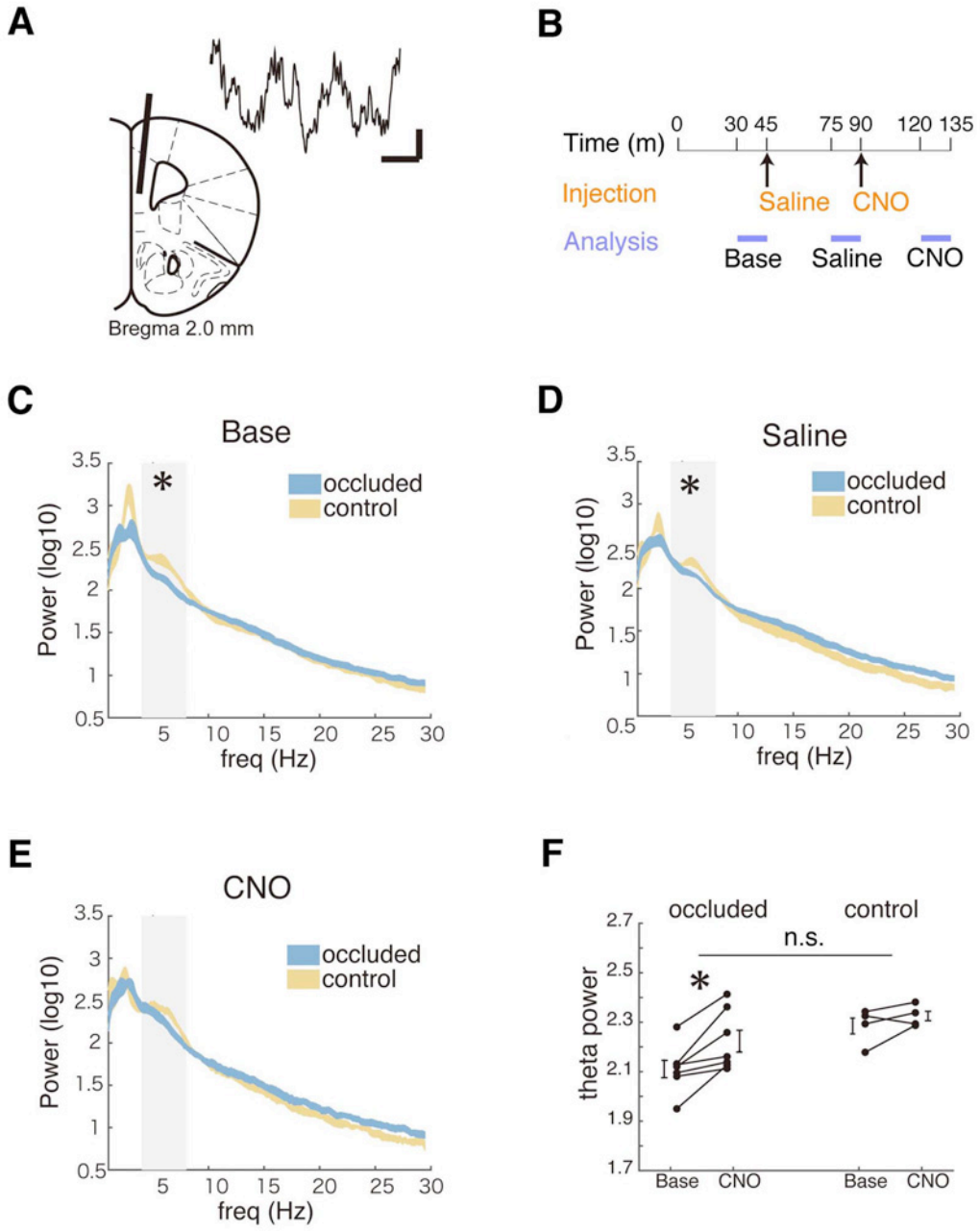

Supplemental Figure 16.

The local field potential (LFP) of the medial prefrontal cortex (mPFC) was analyzed.

(**A**) Location of electrode tips in the mPFC and a representative local field potential tracing. Calibration: 100 μV, 200 ms.

(**B**) Scheme represents the time-course of the injection of saline/CNO and the recording.

Time indicates the elapsed time after the start of recording. The mice expressing hM3Dq in the mPFC were administered saline and CNO by intraperitoneal injection at 40 min and 90 min after the start of the recording, respectively. Recorded LFP data from 30 to 45 min after the start of recording (Base), after the injection of saline (Saline) and after the injection of saline CNO (CNO) were analyzed.

(**C** to **E**) Power spectrum densities of the LFPs from the mPFC of the mice recorded from 30 to 45 min after the start of the recording (Base, **C**), after the injection of saline (Saline, **D**), and after the injection of CNO (CNO, **E**). The gray areas indicate the theta-band (4-8 Hz). The LFP powers at the theta-band in (**C**) and (**D**) were significantly lower in the occluded mice ($n = 7$) as compared to those in the control mice ($n = 4$). *$p < 0.05$, Mann-Whitney U test.

(**F**) Graph indicates the change of the LFP power at the theta-band. Repeated measures ANOVA revealed no significant effect of CNO treatment between two groups (n.s.), but additional exploratory analysis revealed that CNO treatment potentially increased the theta-band LFP powers of the mPFC significantly in the occluded brains. *$p < 0.05$, Wilcoxon signed-rank test. Bars represent means ± S.E. Each point represents the theta band power of an individual mouse (occluded mice, $n = 7$; control mice, $n = 4$).

Supplemental Figure 17

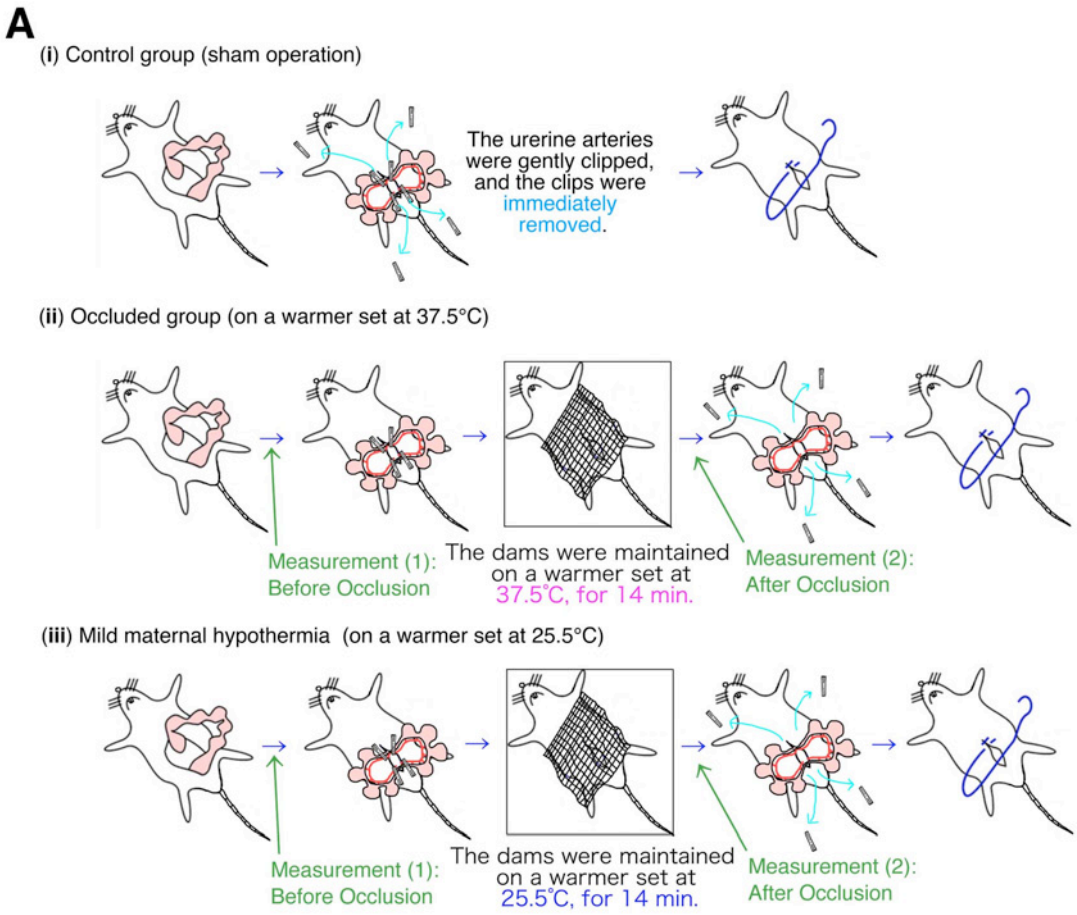

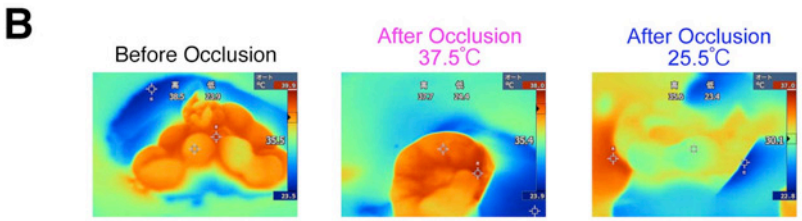

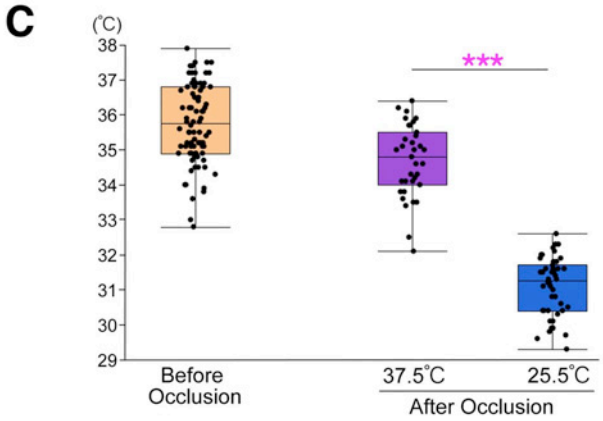

Supplemental Figure 17.

Measurement of the surface temperatures before and after the maternal uterine artery occlusions.

(**A**) Schematic representation of the experimental procedures. In the “(i) control” group, we carried out a sham operation. We exposed the uterine horns, and the uterine arteries were gently clipped, and the clips were immediately removed. In the "(ii) occluded" group, the uterine arteries were occluded with clips, and the dams were maintained on a warmer set at 37.5°C for 14 min, then the clips were removed. In the "(iii) maternal hypothermia" group, the uterine arteries were occluded with clips, and the dams were maintained on a warmer set at 25.5°C for 14 min, then the clips were removed. Surface temperatures of the uterine horns were measured immediately after the uterine horns were exposed (Measurement (1): Before Occlusion). After the maternal uterine artery occlusion on a warmer set at a temperature of 37.5°C or 25.5°C, surface temperatures of the uterine horns were again measured immediately after the uterine horns were exposed (Measurement (2): After Occlusion).

(**B**) Representative images taken by a themography. After the maternal uterine artery occlusion on a warmer set at a temperature of 25.5°C, the surface temperatures of the uterine horns were decreased as indicated by green color (right panel).

(**C**) The measured surface temperatures with a themography are shown (Before Occlusion: $n = 82$, After Occlusion (37.5°C): $n = 35$, After Occlusion (25.5°C): $n = 46$). ***$P < 0.001$, Student’s t-test. Each point represents an individual mouse. Box-and-whisker plots were used to graphically represent the median (line within box), upper and lower quartiles (bounds of box), and maximum and minimum values (top and bottom bars).

Supplemental References

71. Deguchi K, Inoue K, Avila WE, Lopez-Terrada D, Antalffy BA, Quattrocchi CC, Sheldon M, Mikoshiba K, D'Arcangelo G, and Armstrong DL. Reelin and disabled-1 expression in developing and mature human cortical neurons. *J Neuropathol Exp Neurol.* 2003;62(6):676-84.
72. Kaneko Y, Sakakibara S, Imai T, Suzuki A, Nakamura Y, Sawamoto K, Ogawa Y, Toyama Y, Miyata T, and Okano H. Musashi1: an evolutionally conserved marker for CNS progenitor cells including neural stem cells. *Dev Neurosci.* 2000;22(1-2):139-53.
73. Nakamura Y, Yamamoto M, Oda E, Yamamoto A, Kanemura Y, Hara M, Suzuki A, Yamasaki M, and Okano H. Expression of tubulin beta II in neural stem/progenitor cells and radial fibers during human fetal brain development. *Lab Invest.* 2003;83(4):479-89.
74. Nakajima K, Mikoshiba K, Miyata T, Kudo C, and Ogawa M. Disruption of hippocampal development in vivo by CR-50 mAb against reelin. *Proc Natl Acad Sci U S A.* 1997;94(15):8196-201.
75. Tabata H, and Nakajima K. Efficient in utero gene transfer system to the developing mouse brain using electroporation: visualization of neuronal migration in the developing cortex. *Neuroscience.* 2001;103(4):865-72.
76. Tabata H, and Nakajima K. Labeling embryonic mouse central nervous system cells by in utero electroporation. *Dev Growth Differ.* 2008;50(6):507-11.
77. Niwa H, Yamamura K, and Miyazaki J. Efficient selection for high-expression transfectants with a novel eukaryotic vector. *Gene.* 1991;108(2):193-9.
78. Kubo K, Honda T, Tomita K, Sekine K, Ishii K, Uto A, Kobayashi K, Tabata H, and Nakajima K. Ectopic Reelin induces neuronal aggregation with a normal birthdate-dependent "inside-out" alignment in the developing neocortex. *J Neurosci.* 2010;30(33):10953-66.
79. Tomita K, Kubo K, Ishii K, and Nakajima K. Disrupted-in-Schizophrenia-1 (Disc1) is necessary for migration of the pyramidal neurons during mouse hippocampal development. *Hum Mol Genet.* 2011;20(14):2834-45.

80. Lee PR, Brady DL, Shapiro RA, Dorsa DM, and Koenig JI. Social interaction deficits caused by chronic phencyclidine administration are reversed by oxytocin. *Neuropsychopharmacology.* 2005;30(10):1883-94.
81. Nagai T, Kitahara Y, Shiraki A, Hikita T, Taya S, Kaibuchi K, and Yamada K. Dysfunction of dopamine release in the prefrontal cortex of dysbindin deficient sandy mice: an in vivo microdialysis study. *Neurosci Lett.* 2010;470(2):134-8.